Investigation of Novel Precursor Routes for Incorporation of Oxynitride Spinel Phases into Ceramic-Metallic Composites Formed via the TCON Process

by

Joshua Denmeade

Submitted in Partial Fulfillment of the Requirements

for the Degree of

Master of Science

in the

Chemistry

Program

YOUNGSTOWN STATE UNIVERSITY

December 2013

Investigation of Novel Precursor Routes for Incorporation of Oxynitride Spinel Phases into Ceramic-Metallic Composites Formed via the TCON Process

Joshua Denmeade

I hereby release this thesis to the public. I understand that this thesis will be made available from the OhioLINK ETD Center and the Maag Library Circulation Desk for public access. I also authorize the University or other individuals to make copies of this thesis as needed for scholarly research.

Signature:

Joshua Denmeade, Student Date

Approvals:

Dr. Timothy Wagner, Thesis Advisor Date

Dr. Daryl Mincey, Committee Member Date

Dr. Ruigang Wang, Committee Member Date

Dr. Salvatore Sanders, Associate Dean Graduate Studies and Research Date

Abstract

Fireline TCON Inc. has developed a process for the production of interpenetrating phase composites consisting of the phases of aluminum and alumina. These composites are formed via a process called reactive metal penetration. TCON composites made by taking precursors that are silica based, and then these precursors are placed inside a molten aluminum, or aluminum alloy bath. The resulting composites have unique physical properties that are a combination of the properties of both the aluminum and alumina phases. These properties can be adjusted by changing the composition of the precursor or the composition of the melt, with the goal of producing specific properties in the composites.

According to research, silica is not the only ceramic that will work with this process. Other teams have transformed titanium with the goal of introducing titanium into the metallic phase. Another option can be to target the ceramic phase to find compounds that will have better bonds with the metal phase. To do that, a possible route is to start finding oxynitride ceramics that will work with the TCON process.

To make these oxynitrides, many different methods were used with varying degrees of success, due to the instability of many of these compounds and the difficulty in keeping them from decomposing. Once formed, these compounds could then be reacted with molten aluminum in one of several ways, with the goal of producing a transparent spinel in the ceramic phase. These samples before and after transformation were examined using Powder X-ray Diffraction, Scanning Electron Microscopy, and Energy Dispersive Spectroscopy.

Acknowledgments

First, I would like to thank my research advisor, Dr. Timothy Wagner, for all of his support in this endeavor. His help constructing apparatuses, providing direction, and all of his other help have proved invaluable. He has left me perfectly equipped for a career after graduation.

Also, I would like to thank other members of the faculty for their support and assistance. Specifically, I would like to thank Dr. Daryl Mincey, Dr. Ruigang Wang, Dr. Matthias Zeller, and Dr. Dingqiang Li. Dr. Mincey and Dr. Wang have graciously agreed to be members of my thesis committee, and have assisted me with many different aspects of my journey at Youngstown State University. Dr. Zeller has been instrumental in the analysis of all the powder patterns seen in this thesis. In addition, he provided instruction on many different methods used for the X-ray diffractometer, in both the instrument and the preparation of samples. Dr. Li has provided help in the instruction of the use of the Scanning Electron Microscope, in addition to assisting with preparation of samples.

Also, I wish to acknowledge Kyle Myers, a former student in the Wagner group. Certain sections in Chapters 1 and 4 in this thesis have borrowed from Kyle's work (MS Thesis, May 2012), and access to his insight and experience gained through his related project are greatly appreciated.

The Chemistry Department a Youngstown State University also deserves to be thanked, due to their endless support of my journey. They have provided advice, knowledge, and were gracious enough to present me with the Dr. James A. Reeder Graduate Scholarship Award. And for all those things, I am eternally grateful.

Finally, I would like to thank my parents, my family, and my girlfriend for their support. Without them supporting me when I needed it, I would never have been able to make it to where I am today. I love you all.

Table of Contents

List of Figures

Table of Tables

Chapter 1

Introduction to Interpenetrating Phase Composites and the TCON Process

1.1 Interpenetrating Phase Composites

Since the 1970's, when advanced composite materials were placed into common use, there has been a high demand for new and unexplored composites due to their extraordinary and interesting mechanical properties. Interpenetrating phase composites (IPCs) are the focus of this thesis. An IPC is a type of composite that features two or more materials combined into a three dimensional matrix. The benefit of this type of system is that each individual system adds its own properties to the properties of the entire system. This provides a synergistic effect where the composite is more than a summation of each individual system, and often times these characteristics can be designed with specific properties in mind. The types of composites most often studied, and those that are the focus of this thesis, are a combination of metallic and ceramic phases. In these composites, the metal phase contributes properties such as electrical and thermal conductivity, and good toughness [1], whereas the ceramic phase contributes high stiffness, low density, and excellent refractory properties, e.g. resistance to corrosion and erosion at high temperatures. One of the most studied systems is a composite comprised of aluminum in the metallic phase and a ceramic phase consisting of alpha alumina (α-alumina, Al_2O_3). This IPC is known for its outstanding mechanical properties of resistance to corrosion at elevated temperatures, toughness, as well as increased wear properties when compared to other ceramic materials [2]. Even though much progress has been made with these materials, research continues, so that the properties of these materials can be tuned for specific purposes, and increase specific properties such as toughness, hardness, and wears resistance [3].

One of the methods that have been used to create these IPC systems is a method known as reactive metal penetration (RMP) [4], which will be the focus of this thesis. This method uses molten metal to perform a liquid-solid displacement reaction using an oxide that is known as the sacrificial oxide. This sacrificial oxide is displaced to make room for the new α-alumina phase by initially forming an oxide layer on the surface of the preform, and then the reaction works through the preform layer by layer. During the reaction, molten metal must be continuously supplied to the system, and this is delivered

through the channels formed during the displacement of the sacrificial oxide. These channels are formed due to the smaller relative volume and higher density of the formed oxide when compared to the sacrificial oxide. After the reaction is completed, these channels will be occupied by the excess metal. This process will be referred to as "transformation" throughout this thesis. The process is termed a near-net shape reaction because once the reaction goes to completion there is a reduction of size of only about 1%.

The first instance of a reaction that would later lead to the formation of Al/Al_2O_3 IPCs was in the containment of molten aluminum in SiO_2-based ceramic vessels. In the 1950's there were reports of detrimental reaction in the silica based refractories that were used to contain molten aluminum that would compromise the performance of these vessels [5]. Due to this observation, it was discovered that the aluminum reacts with the silica to form the alumina and metal aluminum composite with silica in the matrix as well, and this reaction was energetically favorable above 760°C. This was later proven when other research showed that the Gibbs free energy value for the reaction was negative. The first patent for any process related to RMP was given to Henri George in 1955 [6]. The patent covered any reaction involving silica reacting with any reducing metal to form a material that has characteristics of both metals and ceramics. The general reaction provided in the patent is given in Equation 1.1

$$SiO_2 + M \rightarrow MSi_n + MO_x \qquad \text{Equation (1.1)}$$

Equation 1.1 shows that in the presence of a reducing metal, represented by M, silica will react to form a metal-silicon alloy MSi_n and metal oxide MO_x, where the subscript n shows the ratio between the metal and the silicon that can be varied. According to George's patent, this reaction works best between 700 and 900°C, because at temperatures above 1000°C, the grains of alumina will be larger. The size of the alumina grains is known to have a direct correlation to the mechanical properties of a composite. Also this patent included the observation that the RMP process made near net-shape ceramic-metal composites. Though this process showed many industrial applications, no

serious research was completed on utilizing this technique until Breslin started reinvestigating its use in 1993 [7].

In 1993, Michael Breslin published a patent that employed the submersion of a sacrificial ceramic preform in a bath of molten metal [7]. The process used involved temperatures ranging from 1000 to 1200°C, which is notable due to these temperatures being much higher than the process described by George. This patent is also the first patent related to RMP to mention that both phases in the composite are co-continuous. These composites are said to be 70% ceramic phase and 30% metal phase, which puts these in a class called ceramic matrix composites (CMC). This technique preferred to use silica for the ceramic preform and aluminum as the reducing metal. When temperatures are higher than 950°C, silica is known to react with aluminum via the following reaction shown in Equation 1.2.

$$(4 + x)Al + 3SiO_2 \rightarrow 2Al_2O_3 + 3[Si]Al + xAl \qquad \text{Equation (1.2)}$$

This equation shows that the excess aluminum is what will push the reaction forward, denoted by x. This reaction will occur at any temperature that is above the melting point of aluminum. But, the reaction will only produce a co-continuous network of α-alumina and aluminum if the temperature is above 950°C [8]. While many different systems could produce an IPC, it is important to note that silica is the most studied compound for this reaction to form the Al/Al_2O_3 system.

Köster and Liu [1] reported that there are three conditions required, but not necessarily sufficient, for the transformation process described in Breslin's patent to work. The conditions are as follows: 1) the oxide being created must have a smaller specific volume than sacrificial oxide, 2) the oxide being created must have a higher negative Gibbs free energy value (ΔG), such that the formed oxide is more energetically favorable at the specified temperature and under the specific molten metal conditions, and 3) the temperature of the reaction must be above the melting point of the reducing metal, but below its boiling point as well as below the melting points of both the sacrificial oxide and the oxide being formed. Figure 1.1 illustrates these criteria.

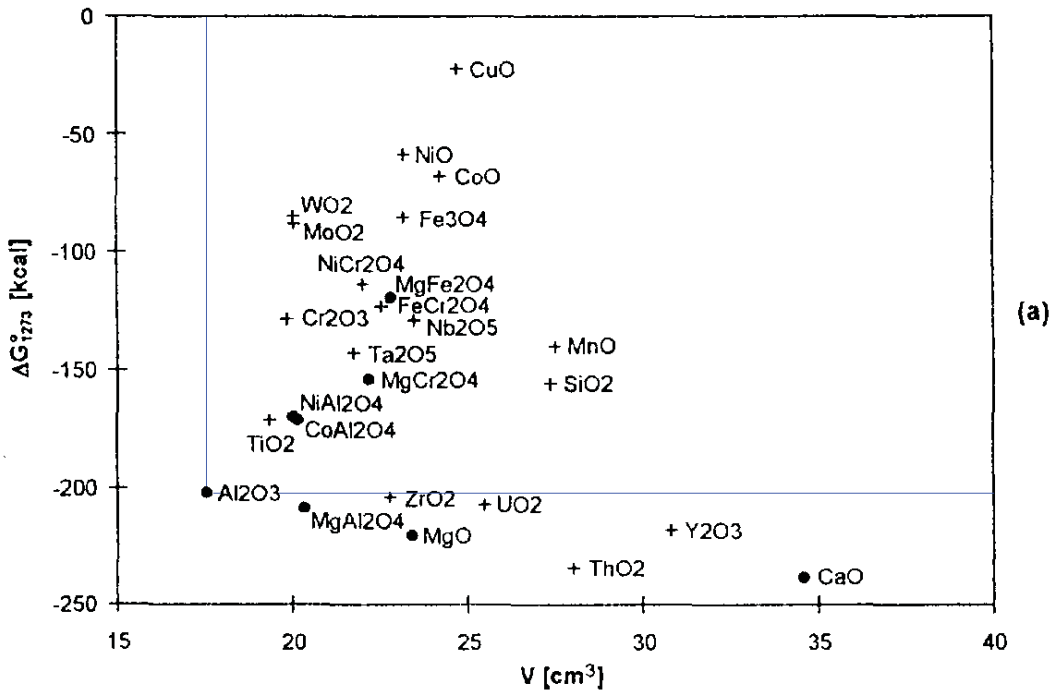

Figure 1.1 Formation-Condition diagram at 1000 °C for the RMP process. Volume is on the x-axis and on the y-axis is Gibbs free energy. Anything contained within the blue box is considered energetically favorable for the formation of the alumina/aluminum system. Figure taken from Köster and Liu [1].

The plot in Figure 1.1 shows the relationship between Gibbs free energy and specific volume for ceramics at 1000°C. The blue box, which has been edited-in, shows the minimum values for both specific volume and Gibbs free energy needed to be able to form alumina. This means that, in theory, any of the oxides in the blue box would be able to react with aluminum metal at 1000°C with the resulting compound being comprised of alumina. These two variables plotted in Figure 1.1 are considered the two most important governing the reaction. Gibbs free energy is so important due to spontaneity. If the reaction does not have a negative Gibbs free energy value, then it will not be viable thermodynamically. This can be overcome by the "addition" of extra energy into the system, which would reverse the direction of the reaction, but, from a real world perspective, it makes the entire process much less practical and applicable. This is important for companies who are targeting specific markets with specific products. Volume is also important due to the nature of the reaction. If the formed oxide is larger than the sacrificial oxide, there will be no room for the aluminum to penetrate into the

sacrificial oxide, which would then show itself as a very limited reaction. Even if there was penetration however, there would be no channels left unoccupied that the aluminum could settle into, creating the co-continuous network. This process of creating alumina, which creates channels for the aluminum to penetrate deeper into the preform, is referred to by Breslin *et al.* [8] as "cracking", and is depicted in Figure 1.2

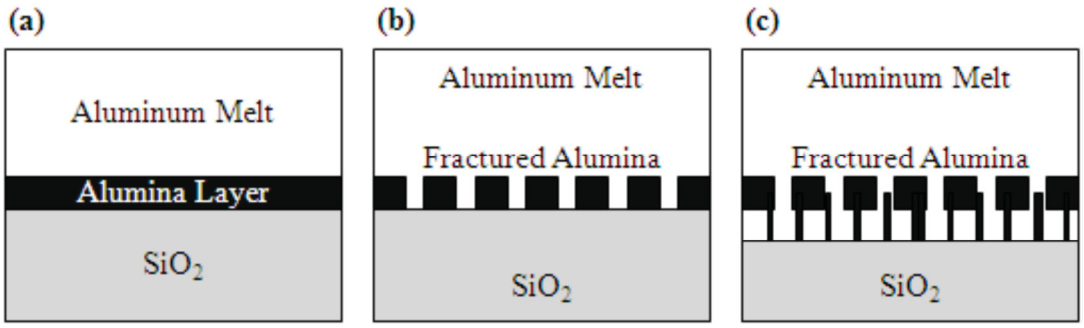

Figure 1.2 Breslin's proposed formation mechanism. (a) Liquid aluminum contacts the SiO_2 preform and an alumina layer is formed. (b) At a critical thickness the alumina layer "cracks" allowing liquid Al to progress through and continue the reaction. (c) The reaction continues and results in a co-continuity of both phases. (Figure adapted from Breslin *et al.*[8])

1.2 Wetting of Oxide Preforms with Aluminum

A good example of the fact that these three important factors listed by Köster and Liu are not the only important factors is the difference between the reaction rates for SiO_2 and TiO_2. While both SiO_2 and TiO_2 are listed inside the blue box in Figure.1.1, SiO_2 will readily transform into the composite, while given similar temperatures, reaction conditions, and amount of time, TiO_2 will only have a small amount of alumina formed on the surface. Even though the reaction between TiO_2 and aluminum at 1000°C is thermodynamically favorable and the conditions theoretically indicate that the reaction should work, there are other factors that inhibit this reaction. This shows that while the conditions listed above are important for the formation of the Al/Al_2O_3 composite, they are not in themselves sufficient for the reaction to move forward. One of these reasons that may limit how the TiO_2 and the aluminum interact is due to how the aluminum wets the TiO_2. It has been demonstrated by several authors that TiO_2 is very poorly wet by aluminum at the temperatures that are used for the RMP process [9-12].

Wetting is described as the ability of a liquid to maintain contact with a solid surface. The degree to which something is considered to be wet is determined when the cohesive and adhesive forces of the solid and liquid interact due to contact between the two. Chidambaram *et al*. [13] describes wetting in two general categories: 1) physical wetting, where the reversible physical forces, such as van der Waals forces, provide the attractive energy required to wet the surface, and 2) chemical wetting, where a reaction occurs between the two surfaces, and the bonds that result from this are in control of the wetting. Chidambaram *et al*. then go on to discuss that metals wet ceramics via a chemical wetting process. The wetting is considered good if the contact angle θ is less than 90°, with θ being the angle between the vectors τ_{LV} and τ_{SL}. This is exemplified is Figure 1.3.

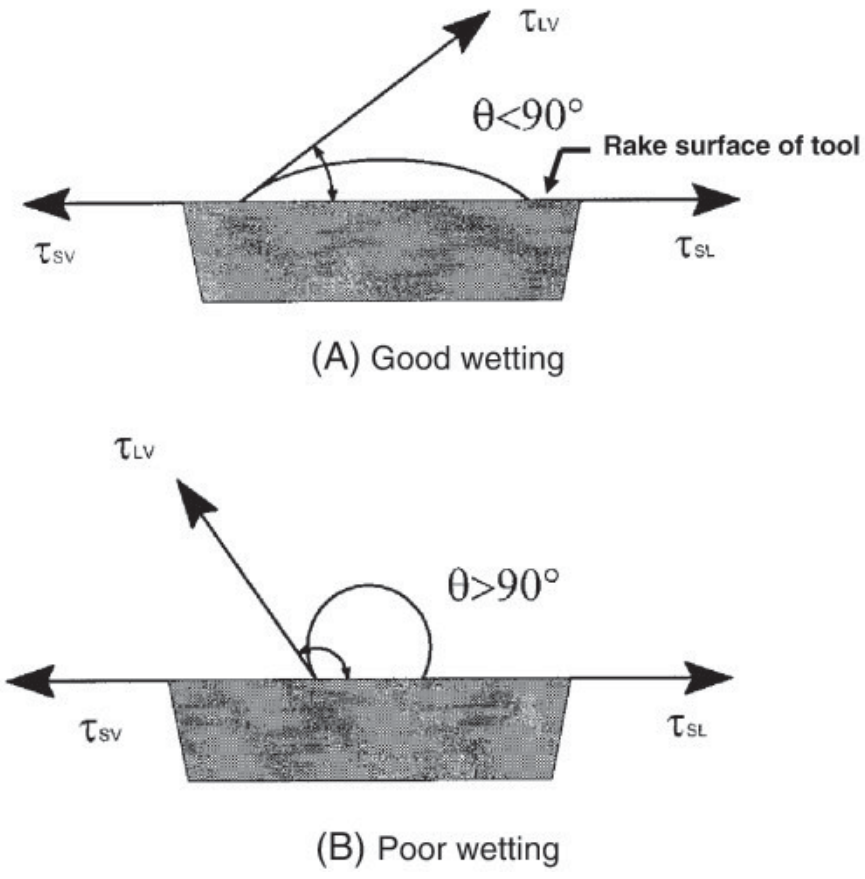

Figure 1.3 Example of good wetting (top) and poor wetting (bottom) [14]

Figure 1.3 shows an example of good (top) and poor (bottom) wetting behaviors. This corresponds to Equation 1.3 where τ_{SV}, τ_{LV}, and τ_{SL} are vectors representing the surface energies of solid/vapor, liquid/vapor, and solid/liquid interfaces, respectively.

$$\tau_{LV}\cos\theta = \tau_{SV} - \tau_{SL} \qquad \text{Equation (1.3)}$$

The reaction of aluminum wetting a variety of ceramics was expounded upon by Sobczak *et al.* in several different publications [12, 15-18]. Experiments done by this group include the wetting with molten aluminum of $B_{13}O_2$, NiO, CoO, ZnO, TiO_2, SiO_2, ZrO_2, and fly ash. To demonstrate the difference between the example used in the previous section, SiO_2 and TiO_2, their angles of wetting are presented in Table 1.1.

Table 1.1 Wetting angles of aluminum metal on SiO_2 and TiO_2 at various temperatures. SiO_2 data was taken from Sobczak *et al*. [17] and TiO_2 data was taken from Sobczak *et al*. [18].

Substrate	Temperature (°C)	Time (min)	θ (°)
SiO_2	800	120	112
	900	120	88
	1000	120	53
TiO_2	900	120	96
	1000	120	80
	1100	120	64

When looking at the values for θ, TiO_2 has what would appear to be a good wetting angle of 80°. This is under the 90° benchmark, and would be considered good conditions for wetting. But when it is compared at the same temperature with SiO_2, it is observed that the angle is much greater than the angle for SiO_2 (θ = 53°). Actually, when transformed in aluminum utilizing the so-called TCON process (see next section) used in the work in this thesis, the reaction appeared to be very slow, and in most cases stopped after minimal transformation [19].

One possible reason that these compounds wet so differently could deal with the fact that there is a stark difference between SiO_2 and TiO_2 in terms of relative volume when compared to alumina, as can be seen in Figure 1.1. This would mean that when the

SiO_2 is reacting to form Al_2O_3, it is forming larger channels in the matrix, which is what allows the aluminum to penetrate into the ceramic preform and continue the reaction. These factors are important to look as to compare the ceramic preforms being considered for transformation. If any of these factors are present, the ceramic will not wet properly, and it will lead to a partial or surface level transformation. TiO_2 provides a good window against which other ceramics can be measured to determine their viability, due to its study and comparison to the most successful system used, SiO_2.

It turns out that TiO_2 will eventually transform in aluminum when given a reasonable amount of time, but only at temperatures much higher than the temperatures used in the SiO_2 reaction. This is most likely due to the higher rates of diffusion at this temperature of the newly formed composite, which allows the reaction to propagate. Also, at the higher temperature, the activation energy of the kinetic reaction constant is lowered [11], which increases the reactive wetting of TiO_2 by liquid aluminum. When compared to the SiO_2 system, this difference in activation energy could explain the slower process for TiO_2. This will be an important factor when looking at the oxynitride species that will be the focus of this thesis. Given that these oxynitride species have not been extensively used for RMP processes, factors such as wetting will have to be extrapolated for these compounds, and as such, examples such as TiO_2 give a good representation of the possible hurdles to be faced using this class of compounds.

1.3 Fireline TCON

The TCON Division of Fireline Inc., located in Youngstown, OH, has developed a unique process for the creation of IPCs using the RMP process. The TCON process is the approach used for creating the IPCs studied in this thesis. This involves taking silica based preforms and then taking advantage of the RMP reaction by plunging the preform into aluminum reactive metal alloys. Currently, the TCON Division produces products that are used by companies for aluminum casting techniques. The R&D department of Fireline has been expanding, attempting to find new techniques to increase specific properties of their products (i.e. wear characteristics, reducing failure rates, etc.), and to find new ways to implement their use. Using these new developments, these new TCON products are garnering interest in the use of force protection for vehicle and body armor

systems [20], as well as the braking systems in the automotive industry [21]. Fireline, in conjunction with REX Materials Group, is trying to get into the market for lightweight brake rotors and ballistic armor.

The reactions performed at Fireline take ceramic preforms and immerse them in large superheated aluminum baths, and sometimes aluminum with silicon added to the melt, at temperatures over 1000°C. Figure 1.6 is a photograph of a Fireline employee loading a ceramic preform into one of the molten metal baths. Following, a photograph showing the difference between the silica preforms and the final corresponding transformed product is shown in Figure 1.7. This gives an example of the near-net shape reaction that is a key part of the TCON process.

Figure 1.6 Molten aluminum furnace at Fireline Inc. in Youngstown, Ohio [22].

Figure 1.7 Ceramic preforms and the corresponding transformed products. On the left of the two pairs is a silica preform prior to transformation. On the right is the product after it has been transformed [22].

The current lines of ceramics for commercial use from the TCON division of Fireline are comprised of alumina/aluminum metal ICPs that are 63% alumina and 37% aluminum and silicon [20]. A micrograph of one of these composites is shown in Figure 1.8.

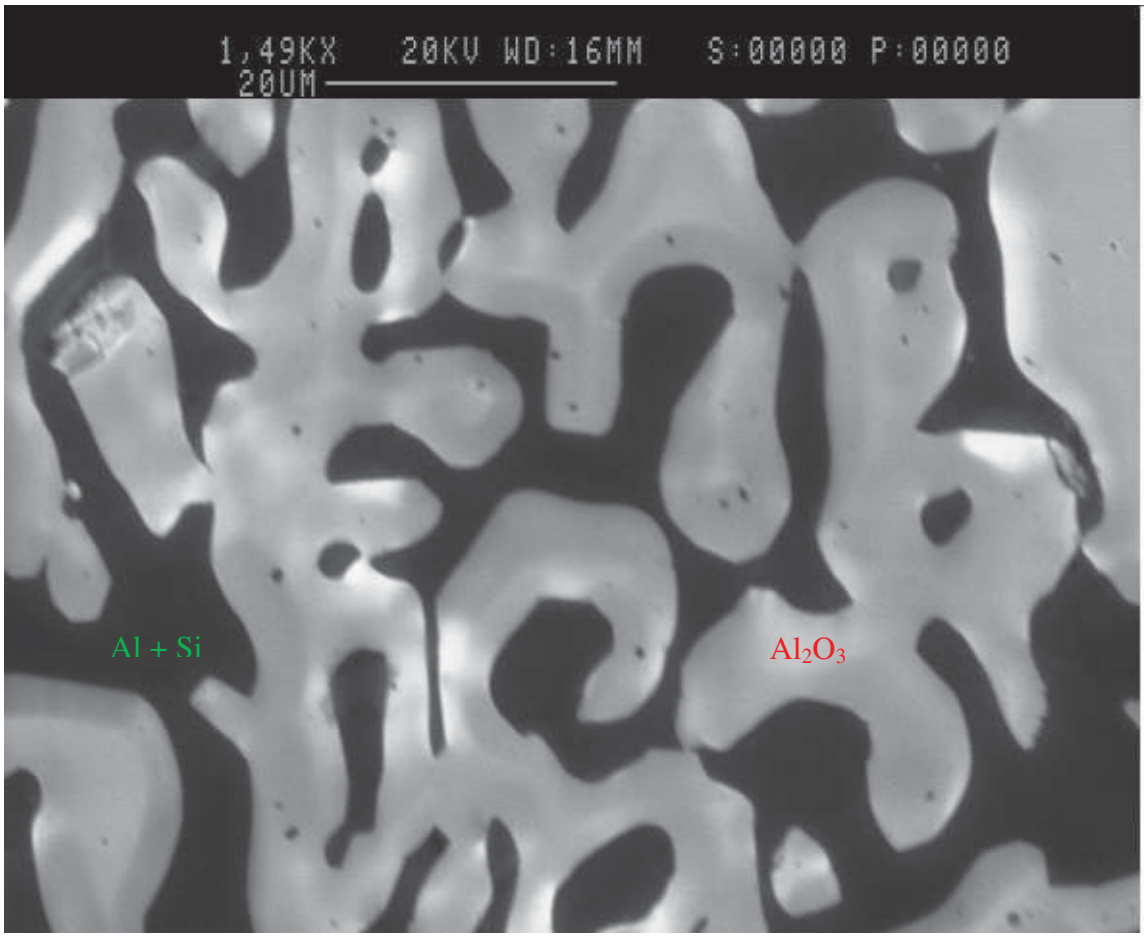

Figure 1.8 SEM Micrograph of TCON material. The darker areas contain the metal alloy while the lighter areas are alumina [22].

A different variant from the silica based composite involves the addition of silicon carbide (SiC) into the ceramic mix while the preforms are being slip-cast. These composites are 53 wt. % SiC, 35 wt. % Al_2O_3, and 12 wt. % aluminum and silicon. The silicon carbide is added to the mix due to these particles being non-reactive under the transformation conditions. This mixing of compounds allows the tuning of properties for composites.

In the next chapter, a comparison of ceramic phases targeted using the TCON process and the research in this thesis, as well as an examination of oxynitride analogs to silica will be discussed.

Chapter 2

Aluminum Oxynitride Ceramics and Sialon as an Analog for Silica

2.1 Aluminum Oxynitride Ceramics

For any RMP reaction using the TCON process, the molten metal reactant phase will usually be a base of aluminum, possibly mixed with silicon or another metal of interest. So, this leaves the ceramic phase as the precursor component that tends to be altered. Different ceramic phases, if able to be transformed via the RMP reaction, would lead to composites systems with potentially unique and enhanced properties. Much of the research that the group performs is centered on incorporating spinel into the ceramic matrix [23], but for this thesis, aluminum oxynitride spinel, referred to as AlON, is the targeted phase. As discussed below, AlON is a generic formula for phases often referred to as "transparent spinels", which are processed for use as optically transparent materials in applications such as bulletproof glass, ballistic glass, and infrared glass for instrumentation. [24]. However, our major interest stems from the cubic crystal structure and attractive material properties of this material for incorporation into an IPC with Al metal.

The junction between the ceramic phase and the metal phase within a ceramic-metallic composite (known as a grain boundary) plays a key role in the strength of the composite. TCON composites typically contain the corundum form of alumina which has a trigonal structure, while the aluminum component is cubic. These different structures result in mismatching of the two phases at the grain boundaries, and as reported in recent work by Moro *et al.* [25] on the Al-Fe composite system, this can be compensated for by the formation of an intermediate nanophase bridging the Al and Al_2O_3 grains. A TEM image depicting such a phase is shown in Fig. 2.1. While such systems do possess high strength [25], it is hypothesized herein that the composite strength could be enhanced even further by incorporating a strong cubic-cubic interface through introducing a cubic spinel as the ceramic phase. Structurally, spinel ($MgAl_2O_4$) and the AlON phases both have face centered cubic lattices, although AlON is an inverse spinel due to the structure having the aluminum ions in both the tetrahedral and octahedral positions, and there is also a disordered vacancy in the spinel octahedral positions in the structures of the γ-oxynitrides, due to cation deficiencies. [26]. Because this structure and aluminum both

have cubic lattices, an interpenetrating phase composite (IPC) containing these phases should be stronger due to the better fit along its ceramic-metallic grain boundaries

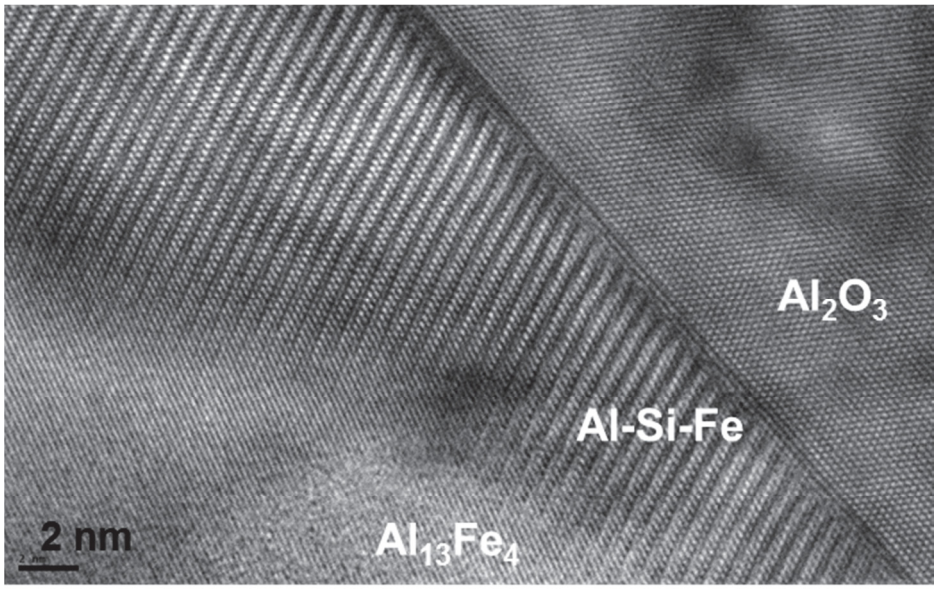

Fig. 2.1. High resolution transmission electron micrograph showing the presence of an Al-Fe-Si alloy nanophase buffering the alumina and Al-Fe grains in an IPC prepared via transformation of a SiO_2 precursor in an Al-7.5wt.% Fe melt [25].

Another reason for targeting AlON as the ceramic component for TCON composites is due to its attractive mechanical properties. The composition of the targeted phase for this thesis is Al_3O_3N, but that is only one of an entire class of ceramics. The AlONs come in many forms, from nitrogen deficient, $Al_{19}O_{27}N$, to nitrogen rich, $Al_{16}O_3N_{14}$ [24]. One common formula for the AlON is $Al_{23-(1/3)x}\ O_{27+x}N_{5-x}$, where $0.429<x<2$, holds true, produced by the manufacturer Surmet [27]. Al Though these compounds differ in formula, they have very similar mechanical properties, with hardness values between 16.5 and 19.5 GPa and strengths of 267 to 306 MPa being reported, depending on the temperature of the system [26]. These measurements show that the AlON is up to 4 times as hard as fused SiO_2, and at least 15% stronger than the related $MgAl_2O_4$ spinel phase [27]. Other important properties include good electrical conduction at elevated temperatures (>1000°C), and the resistance to acids, bases and water. The only area of concern is the oxidation of these oxynitrides. In an oxygenated

atmosphere, the AlON can react with excess amounts of oxygen to produce alumina, as shown in Equation 2.1.

$$4Al_{23}O_{27}N_5 + 15O_2 \rightarrow 46Al_2O_3 + 10N_2 \qquad \text{Equation (2.1)}$$

If this reaction were to take place in a composite, it could greatly increase the failure rate of the system, however this should only occur in an environment where the oxygen content is above atmospheric levels. Also, until a composite containing the oxynitride is formed, the prolonged exposure of the composite to oxygenated atmospheres cannot be studied.

2.2 Silicon Aluminum Oxynitride

Silica has been the most utilized precursor for RMP reactions, due to its ready reaction with molten aluminum. This in turn has led to research that has well-characterized the aluminum/alumina interpenetrating phase composite system [1,2,8,28,29]. The preparation of an aluminum oxynitride ceramic phase via RMP ideally requires a silicon oxynitride, or closely related material, as an analog to the silica used in the transformation reaction to form Al_2O_3. Silicon aluminum oxynitrides, also called Sialons, would seem to be a perfect fit in seeking such a class of compounds.

The first Sialon was reported in the 1970's [30] from the pressing together of aluminum oxide and aluminum nitride with a β-silicon nitride by the following equation listed in Equation 2.2.

$$(2 - z/3)\beta\text{-}Si_3N_4 + (z/3)AlN + (z/3)Al_2O_3 \rightarrow \beta\square\text{-}Si_{6-z}Al_zO_zN_{8-z} \qquad \text{Equation (2.2)}$$

These compounds are called either an α- or β-sialon based on the crystal structure in comparison to the structure of either α- or β-silicon nitride [30-32]. Specifically, the α-silicon nitride, and by extension the α-Sialon, possess a trigonal crystal structure, while the β-silicon nitride and the β-Sialon possess a hexagonal crystal structure. These β-sialon ceramics have been well investigated since their discovery, and are widely used as wear parts, weld location pins, and extrusion dies [30]. There are other types of Sialons, but for

the purposes of this thesis, the β-sialon is the phase that is worth taking a look at due to the lack of industrial uses for the α-sialon. β-sialons can be produced in many ways, such as: sintering pressed powdered mixtures, carbothermal reduction of aluminosilicates in nitrogen, sol-gel processing, and combustion synthesis [33]. Many of these methods create products that are multiphase ceramic mixtures rather than pure single phase ceramic compounds.

Navrotsky *et al.* [33] outline a new approach for the synthesis of β-sialons, involving using a mixture of silicon nitride, aluminum oxide, and aluminum nitride ground together and placed inside a graphite die. A 25 V/750 Amp direct current electrical pulse was then applied to the mixture for 90 ms on/off in cycles for a total time of one minute. Complete reaction to the β-sialon, $Si_{3.17}Al_{2.83}O_{2.83}N_{5.17}$, occurred, as indicated by comparison of the via powder X-ray diffraction (PXRD) patterns of the final product versus the starting materials. The pure state of the sialon then allowed better analysis of the different thermochemical parameters of the material in the course of the study. .

Alpha-sialons, while not nearly as important as β-sialons in terms of applications [32], prove to have an interesting characteristic that leads to a possible route for their use in experimentation. G. Cao and R. Metselaar [30] report that when forming α- and β-sialons, a phase transition between the two will not take place, although conversion from one phase to the other could possibly occur by the chemical reactions shown in Equations 2.3 and 2.4.

α-sialon + oxide → β-sialon Equation (2.3)

β-sialon + nitride → α-sialon Equation (2.4)

These specific transformations have been observed in systems for the Ca-α-sialon, and the Y- α-sialon. This technique could be used as a possible backup if no useful β-sialons could be synthesized, but an α-sialon were readily available.

Q. Qiu *et. al* [32] have done research on the synthesis of the β-sialon phase after discovering that the β-sialon was more likely to be stable than the α-sialon, since β-silicon nitride is more stable than the α-silicon nitride. The goal of the project was to

lower the cost of these sialons by using different sources of aluminosilicates, including clay, kaolin, volcanic ash combined with aluminum powder, rice husks, coal, and finally fly ash. Their proposed reaction using fly ash is shown in Equation 2.5.

$$3Al_2Si_2O_5(OH)_4 + 15C + 5N_2 \rightarrow 2Si_3Al_3O_3N_5 + 6H_2O + 15CO \qquad \text{Equation (2.5)}$$

Four grams of the fly ash sample was reacted under nitrogen flow in a tube furnace at 1400°C. The resulting powder was examined using PXRD, SEM and TEM, showing that a nearly pure β-sialon phase could be produced at 1300°C. Also, they found that if they altered the conditions, they could control the nitrogen content in the compound.

These different syntheses routes show that there are several various methods by which these sialons can be formed, and many different stoichiometric representations within the class of sialon compounds.

Chapter 3

Statement of the Problem

3.1 Objectives and Purpose of Research

The major goal of the overall research is to produce novel ceramic metallic composites via the TCON process using unique ceramic precursors to achieve enhanced mechanical properties. Unique ceramic precursors for this purpose are materials that have not yet been used as a preform in the TCON reactive metal penetration process (RMP), and these include both novel as well as previously reported compounds. .

The main objective of this specific research project is to successfully synthesize oxynitride compounds and use them as precursors to create composites via the TCON process. The ultimate goal is to incorporate the aluminum oxynitride (Al_3O_3N) phase into a composite. Aluminum oxynitride is a cubic spinel material, and is more commonly known as the 'transparent spinel' used for armor applications and for its excellent optical and mechanical properties [26, 34-36]. For example, it is over 10% harder than $MgAl_2O_4$ spinel [37]. A guiding hypothesis of this thesis is that a cubic spinel-cubic Al interfacial epitaxy will result in relatively strong bonding compared to the trigonal Al_2O_3 – cubic Al interface in typically prepared IPCs. This, coupled with the superior mechanical properties of Al_3O_3N, should lead to a stronger, lightweight composite system.

Preforms that show successful complete transformation in initial investigations will be scaled up into test bars and the mechanical properties will be tested. After testing, comparisons will be made between the new preforms and the current Fireline TCON products.

3.2 Unique Precursors for Synthesis

The proposed unique oxynitride ceramic precursors targeted for synthesis in this thesis are listed in Table 3.1. If successfully prepared, these precursors will be transformed in molten aluminum using the TCON process, with the goal of forming new interpenetrating phase composite materials.

Table 3.1 List of targeted precursors for synthesis and transformation, along with targeted composite composition

Targeted Precursor to be Synthesized	**Previously Reported?**	**Targeted Composite Composition**
$SiAl_2O_2N_2$	Yes [38]	Al_3O_3N/Al
$SrSi_2O_2N_2$	Yes [39]	Al_3O_3N/Al
Fe_3O_3N	No	Al_3O_3N/Al
Fe_2AlO_3N	No	Al_3O_3N/Al

Chapter 4

Experimental Methods

4.1 Transformation Techniques

4.1.1 Transformation via the TCON Process

The precursor materials synthesized for this thesis were pressed into pellets that were about a quarter of an inch thick and had a diameter of a half an inch. These pellets were uniaxially pressed to approximately 3000-3500 psi and held for 30 seconds to 1 minute using a steel die press. These pellets were then taken to Fireline, and placed inside a silica based crucible produced there. This crucible is made from a type of silica slurry that is part of Fireline's line of products for the containment of molten metals. This silica is slow to react with aluminum at high temperatures, making it ideal for containing pellets for the RMP process, because this limits possible side reactions occurring in the melt. These crucibles are designed for the RMP process, and have three holes in the side, large enough to let liquid metal in, but small enough to keep the pellets from floating out. The top of the crucible is topped with a plug made of the same material. This stopper keeps the pellet from floating out, if the density of the precursor would allow it to float in the liquid aluminum. An excess amount of aluminum metal is weighed out and placed in a larger crucible of the same silica mix as the first. These two crucibles, the one containing the metal and the one containing the pellet, are heated up to the target temperature in separate, small scale LL Kilns, a photograph of which can be seen in Figure 4.1.

Figure 4.1 Photograph of small scale LL Kilns used for laboratory transformations.

This prevents thermal shock from cracking or destroying pellets, which would happen if the pellets were placed in the aluminum melt at room temperature. This would render the sample useless, and so these pellets are ramped up separately. When both kilns have reached the desired temperature, normally between 1100-1200°C, the crucible containing the pellet is moved to the kiln with the aluminum melt, and placed inside the crucible with the aluminum for the duration of the transformation. To prevent the oxidation of the aluminum metal, the crucibles are kept under a constant flow of argon. After the desired transformation time, the crucible containing the pellets is removed and the pellets are removed and allowed to cool to room temperature. The immediate removal of excess metal is not necessary, because it will later be removed for characterization. An important thing to note is that while the kilns are open, reflective thermal coats, gloves, and a tinted face shield must be worn for protection from the high temperatures.

4.1.2 Transformation via Box Furnace

The ceramic phase being targeted for this thesis doesn't form under 1350°C, and so a different approach to the transformation process was pursued as the kilns only safely go up to 1200°C. So the first approach used was to attempt an even smaller scale

transformation in a box furnace. Both the pellet and a crucible were placed in a box furnace. The crucible is filled with an excess of aluminum. The box furnace is set to 1390°C. Once the furnace has reached temperature, the furnace is opened, and the pellet is placed inside the crucible, and a cap is placed over the crucible to keep the pellet in the aluminum, in case it floats. After the desired transformation time, the crucible is poured out onto a tray made to handle molten metal. The pellet is then removed from the puddle of molten metal on the tray. Just as with the process in Section 4.1.1 of this chapter, anytime the door to the furnace is open, protective equipment must be worn. Photographs for this process can be seen in Figures 4.2, 4.3 and 4.4.

Figure 4.2 Removal of crucible and sample pellet from the box furnace

Figure 4.3 Pouring out the molten aluminum and sample pellet from crucible.

Figure 4.4 Cooling aluminum after being poured out onto tray. Sample pellet is on the middle of the tray.

4.1.3 Transformation via Tube Furnace

Another method for the smaller scale transformation was to use a tube furnace in a similar manner as the box furnace. For this method, however, the system cannot be readily opened as with the box furnace. So, there will be no opportunity for a separate heating before the combination of the metal and ceramic. The crucible will be placed inside the tube furnace with the pellet in the bottom of the crucible and a block of aluminum on top of the pellet. The furnace is then ramped up to 1450-1600°C at the fastest rate possible, and then held there for the desired transformation time. During the whole process, the system is kept under N_2 to keep air out of the system. After the transformation, the crucible is removed and broken to free the pellet and aluminum block from the crucible.

4.2 Characterization of Transformed TCON Materials

4.2.1 Grinding and Polishing

The pellets that are transformed using the TCON technique are characterized using a variety of techniques. For any of these characterization techniques to be used, the pellet must be ground flat. The first grinding is done on a rotating magnetic wheel that has a diamond embedded grinding disk attached via a magnet. Water is used as a lubricant and a coolant. Initially, a 120 grit diamond pad is used, and once ground with that, a 600 grit pad is used. This leaves the pellet with a finish of ca. 30 microns. Each individual pad was used for about 2 minutes. Mechanical polishing is then continued with a diamond suspension using the appropriate cloths until the pellet is left with a finish of 6, and then 3 microns. Finally, the last polish is done using a colloidal silica polish that has a particle size of 0.04 microns. Every sample is washed between steps with soap and water, to prevent cross contamination. Also, between different polishing cloths, the sample is cleaned ultrasonically with acetone to remove any remaining contamination or any contamination that could be remaining on the surface or in the pores of the composite. The procedure is summarized in Table 4.1.

Table 4.1 Procedure for grinding and polishing samples after transformation

Step	Disk Type	Suspension	Lubrication
Grinding 1	Struers Diamond Piano 120 grit	None	Water
Grinding 2	Struers Diamond Piano 600 grit	None	Water
Polish 1	Struers DP-Plan Cloth	Struers 6 μm diamond DP-Suspension	Struers DP-Lubricant Blue
Polish 2	Struers DP-Dac Cloth	Struers 3 μm diamond DP-Suspension	Struers DP-Lubricant Blue
Final Polish	Struers OP-Chem Cloth	Struers colloidal silica OP-Suspension	Water for final 30 seconds

4.2.2 X-ray Diffraction

After grinding and polishing is completed, the sample is analyzed using Powder X-Ray Diffraction (PXRD) to identify what phases are present in the material. As long as the sample is microcrystalline in nature, PXRD analysis can be used regardless of whether it is a powder or a solid sample such as a ceramic-metallic composite surface. The PXRD patterns obtained in this project were collected using a Bruker D8 Advance diffractometer, which uses Cu-K_α radiation as an X-ray source. Sample cups are available for the diffractometer that are of sufficient depth to accommodate the pellets after cutting and polishing, and there are shallower cups that can be used for samples comprised of a powder as well. These cups serve to keep the samples level and at a specific height relative to the diffractometer. The pellet is mounted in the center of the sample cup using paraffin wax. Diffraction patterns were collected at room temperature in reflective mode in Bragg-Brentano geometry. Each sample was run for 3 hours in a range of 10-90° in 2θ. Once the data was collected, it was analyzed and fitted to database patterns using the EVA application version 7.001 software of SOCABIM (1996-2001), distributed by

Bruker AXS. A schematic of Bragg-Brentano geometry as used in the Bruker D8 diffractometer is shown in Figure 4.5.

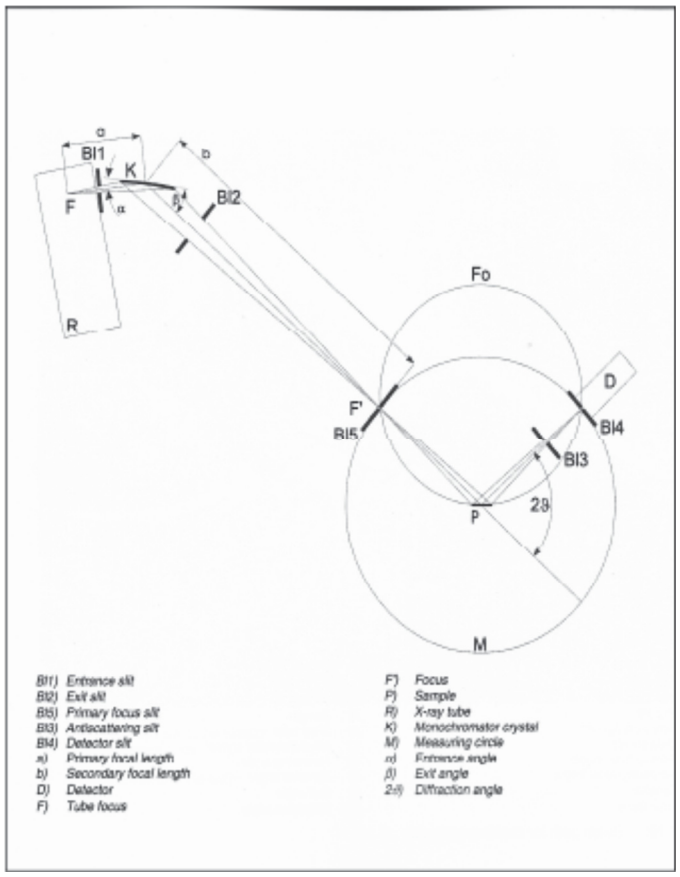

Figure 4.5 Schematic for a Bruker D8 diffractometer in Bragg-Brentano geometry [30].

X-ray beams are generated by the x-ray tube and then diffracted by a monochromator crystal, creating a focused beam of x-rays that are monochromatic. The monochromator focuses the x-rays to pass through a slit. This ensures that the outer parts of the beam are cut off and the x-rays coming out are monochromatic. The x-rays then reach the sample and diffraction takes place. These incident beams are diffracted through destructive and constructive interference following the interactions with the electrons in the crystal lattice. These diffracted x-rays then leave the sample and go through two slits before finally reaching the detector. The constructive interference that can occur between the diffracted waves results in a peak at that specific angle, and is recorded as 2θ. This angle of constructive interference is related to Bragg's equation, shown in Equation 4.1.

This equation is used to determine the interplanar spacings of the planes in the crystal lattice, also called d-spacings.

$$n\lambda = 2d \sin(\theta) \qquad \text{Equation (4.1)}$$

In this equation, n = integer (1, 2, 3…n) related to the order of diffraction, λ = wavelength of the x-rays used, d = the interplanar spacings of the lattice planes, and θ = the angle of incidence of the x-ray beam [31].

These resulting patterns from collection are a plot of intensity vs. 2θ. Using the International Center for Diffraction Database (ICDD), which contains more than 140,000 different compounds and the correlating patterns, these data sets can be analyzed for peak locations. All crystalline materials have unique diffraction patterns because of their distinctive combination of crystal lattice, unit cell parameters, and structure. This allows the matching of peaks in data sets to be matched with peaks from the database, showing which phases are present.

The main goal when performing PXRD analysis is the identification of each individual phase present in a composite. If a compound has no crystalline structure, such as in a liquid, gas, or amorphous compound, then they cannot be detected using X-ray diffraction techniques. This also holds true when particle size is extremely small, such as into the nanometer range, as this is beyond the diffraction threshold, and cannot be detected by XRD analysis. If further characterization is required, scanning electron microscopy coupled with energy dispersive spectroscopy can be used. The PXRD patterns can be further analyzed to give more information such as lattice parameters, space group and structure, crystallite size, and percent composition of phases, depending on what information is needed.

4.2.3 Optical Microscopy

Once a sample is polished and examined using PXRD, it is investigated using optical microscopy. The pellet is mounted on a glass slide using adhesive putty, and then pressed to ensure a level surface for microscopy investigation. The microscope that is used to investigate the composites is a ZEISS Axiophot compound light microscope, seen in Figure 4.6.

Figure 4.6 ZEISS Axiophot compound light microscope

For the acquisition of digital images, a PixelLink® CCD camera is used. For the purposes of this thesis, all images reported are considered brightfield images. This means that the light that is reflected is not altered at all in the creation of the image. Magnifications from x5 to x100 can be achieved. Optical microscopy is the next step after PXRD to see if a transformation has actually occurred, through examining of phases present. These types of reactions could produce multiple phases, but for a transformation to have taken place, a co-continuous network of phases must be present. So, this method shows whether further analysis is necessary, due to either the presence of the co-continuous network, or the lack thereof. Also, one of the other features of this method is that it can be used to

characterize the homogeneity of the composite. With a larger view of the composite, at lower magnification, it is easier to observer macroscopic features such as porosity and homogeneous phases. Even though no chemical analysis or crystallographic information can be gained by optical microscopy, it is still an important step in the analysis so that unique features or phases can be picked out for future analysis, or more detailed analysis.

4.2.4 Scanning Electron Microscopy

The next stage of investigation was analysis using scanning electron microscopy (SEM). The SEM used for this thesis is a JEOL JIB 4500 multi-beam system. Once prepared, samples are attached to a sample holder using two sided, conductive carbon tape. The sample is then inserted into the microscope sample chamber through a vacuum lock, and both secondary and backscattered electron micrographs, as well as EDX and EDS mappings were taken for detailed analysis.

The electrons used for imaging in an electron microscope are created using an electron gun. But, whereas a light based microscope uses mirrors and lenses to focus the beam, an electron microscope uses electromagnetic fields to focus the beam. Once focused, the beam passes through two scanning coils, and this allows the beam to scan a square area of the sample surface [32]. This beam is extremely small, less than 10 nm in diameter. The image is formed in response to collecting the scattered electrons that have interacted with the sample on the surface. As the electron beam interacts with the surface, the electrons can be scattered in either of two ways: elastic or inelastic. For inelastic scattering, these are the secondary electrons that can be used for imaging, while elastic scattering produces backscattered electron images. Other types of interactions that can be detected by the SEM are: cathodoluminescence, auger electrons, and characteristic x-rays. The types of interactions studied in this thesis are secondary electrons, backscattered electrons, and characteristic x-rays for energy dispersive spectroscopy (EDS).

Secondary electrons are the most common imaging technique used for SEM analysis. These electrons are generated from interactions between the electron beam and the electrons on the surface of the sample. The electrons from the electron beam eject the electrons from the atoms in the sample, and these secondary electrons are then collected

for imaging. The electron gun then scans a specific area, and based on the collection of electrons ejected when the electron beam passes over them, an image is constructed.

Backscattered electrons originate from the elastic collisions of electrons with the nuclei of the atoms in the sample. These electrons are then scattered backwards, towards the detector. This technique is useful because the likelihood of an electron being backscattered is proportional to the mass of the atom scattering it. So, the higher atomic mass elements will cause a stronger backscattering effect, and will appear lighter in the micrograph. For compounds that are comprised of multiple elements, this effect is averaged over all the elements in the compound. In a compound comprised of the aluminum/alumina system, the backscattered alumina grains would appear darker than the aluminum, due to the averaging effect between aluminum and oxygen [32, 33]. These micrographs collected via SEM have a magnification range between x10 and x300,000. Figure 4.7 shows the types of interactions between the electron beam and the sample. This picture shows the depths at which the different types of x-rays or electrons are emitted. Low energy electrons, used for secondary electron images are generated in the upper layers. Higher energy electrons, such as those used for backscattered electron images, come from the next layer down, and thus more energy is absorbed by the sample. This means that when a backscattered image is collected, it must be enhanced, and this lowers the resolution of the image [32].

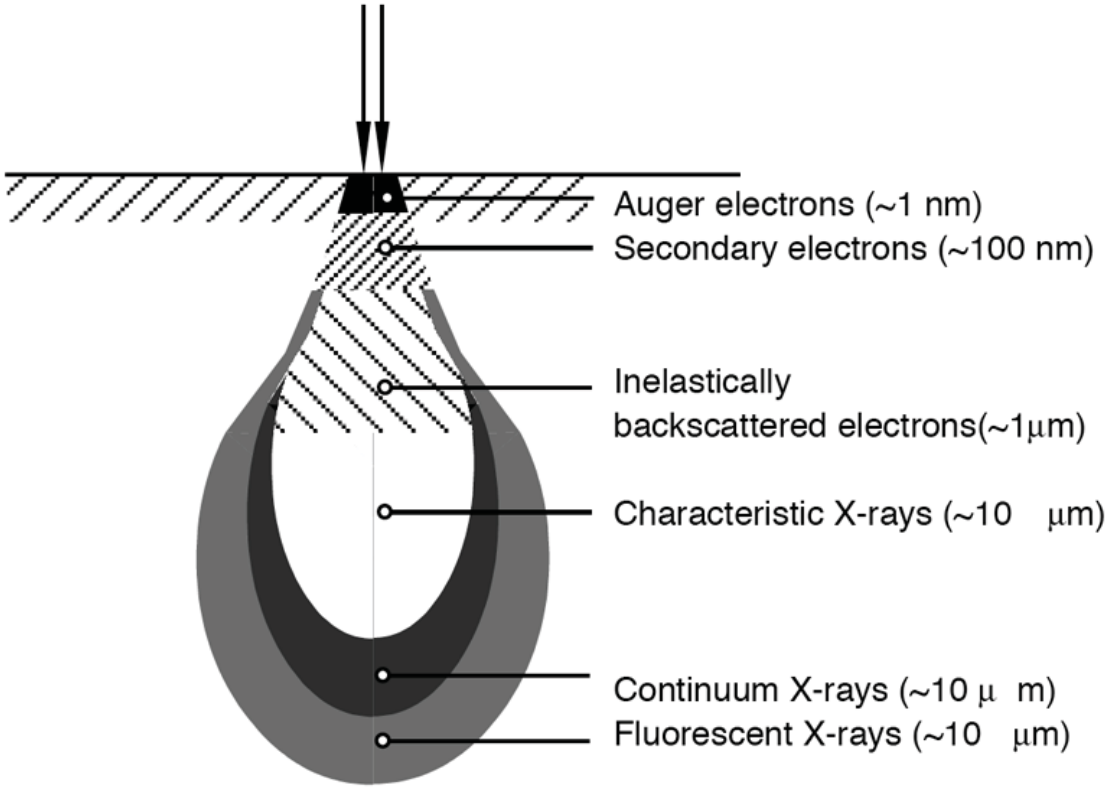

Figure 4.7 Schematic of the interactions of electron beam with any sample material during SEM analysis [34].

4.2.5 Energy Dispersive Spectroscopy

Another facet of electron microscopic investigation is EDS. This technique is used to measure chemical composition and distributions within a sample. An EDAX™ Apollo SDD EDS detector was used in conjunction with a JEOL JIB 4500 multi-beam system to collect the EDS spectra and elemental maps presented within this thesis.

As mentioned in section 4.2.4 of this thesis, characteristic x-rays are generated when the sample is barraged with electrons that penetrate into the sample, as shown in Figure 4.7. This then ejects an electron as shown in Figure 4.8. This electron is assigned a designation depending on what electron shell it is ejected from.

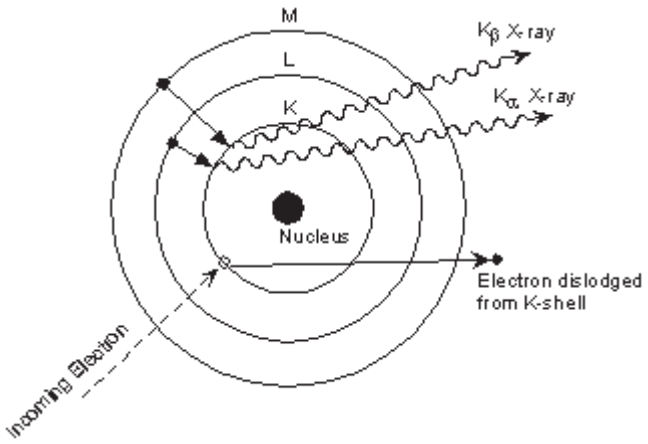

Figure 4.8 Diagram of the generation of K-shell characteristic x-rays [35].

The innermost shell, K, is the most common shell observed for ejected electrons. The ejection of an electron creates a hole in the innermost shell, which will be filled by an electron in a higher shell dropping into this gap, and giving off a photon in the x-ray spectrum as it does. Depending on how many shells the electron has dropped from, the x-ray is given a subscript. If the electron jumped from the L-shell to the K-shell, it is called Kα, and if it came from the M-shell to the K-shell, it is called K_β, and so on.

The wavelengths given off by each element are unique, and can therefore when measured indicate what elements are present in a given area. One technique commonly used with this is called elemental mapping, which shows a distribution of elements for a given area by identifying the different elements present. Each element is assigned a color by the software, and if it is present in greater abundance, it is brighter. Each pixel is eventually assigned a color, and these colors are then grouped together to form phases. These phases can be assessed, which is called phase cluster analysis. For example, if a phase shows that there is a mixture of oxygen and aluminum together, it can safely be assumed to be alumina. These maps can help to more effectively and clearly show the distribution of phases in a material.

4.3 Calibration of Analog Tube Furnace

During the course of experimentation using a tube furnace, a heating coil on the digital tube furnace went out, and a tube furnace with an analog readout had to be obtained. To ensure that proper measurements of temperatures could be reached using

this furnace, it had to be calibrated. To do so, a voltmeter was used with a chromel-alumel thermocouple. The tube furnace was allowed to stay open, and one end of each thermocouple was attached together, while the other end was inserted into the voltmeter. This was then placed into the middle of the furnace, so as to measure the temperature in the hottest area, and where the sample would be placed. Once the reading was obtained from the voltmeter it was compared to the Calibration Tables for Thermocouples for Chromel-Alumel Thermocouples from the CRC Handbook [36]. To account for the temperature already in the room, the temperature outside the furnace was taken and added to any readings obtained from the furnace. A table of these readings can be found in Table 4.2.

Table 4.2 Readings from the voltmeter for the calibration of analog tube furnace [36].

Setting	Voltmeter Reading (V)	Temperature (°C)
0	0.96	24
2	16.93	435.0
3	21.24	537.9
4	28.02	696.0

Thus, for any future experiments, these numbers were used to determine the temperature at which the experiment was proceeding, based upon the number setting of the analog dial.

Chapter 5
Synthesis of Ceramic Precursors

5.1 Fe_3O_3N

Fe_3O_3N has apparently never been successfully synthesized before, but is desirable for this work due to the stoichiometric ratio between Fe_3O_3N and Al_3O_3N, as shown in Equation 5.1.

$$Fe_3O_3N + (x+3)Al \rightarrow Al_3O_3N + FeAl_x \qquad \text{Equation (5.1)}$$

As this compound has never been previously reported, two synthesis routes were formulated for trial, one of which involved the use of a Fe_3O_4 precursor as shown in Equation 5.2, while the other utilized Fe_2O_3 as shown in Equation 5.3. Both of these routes are based on an ammonolysis approach as outlined in Marchand *et al.* [47] for the synthesis of nitrides and oxynitrides from reaction of an original oxide with a dynamic flow of ammonia gas (NH_3).

$$2Fe_3O_4 + 2NH_3 \rightarrow 2Fe_3O_3N + 2H_2O + H_2 \qquad \text{Equation (5.2)}$$

$$3Fe_2O_3 + 2NH_3 \rightarrow 2Fe_3O_3N + 3H_2O \qquad \text{Equation (5.3)}$$

5.1.1 Fe_3O_4

For the first attempt, 1.9732g (8.522 mmol) of Fe_3O_4 was placed in a nickel boat with the powder evenly spread throughout the boat as shown in Figure 5.1. The boat was then placed inside a silica tube, which was in turn placed inside a tube furnace, the setup of which is shown in Figure 5.2.

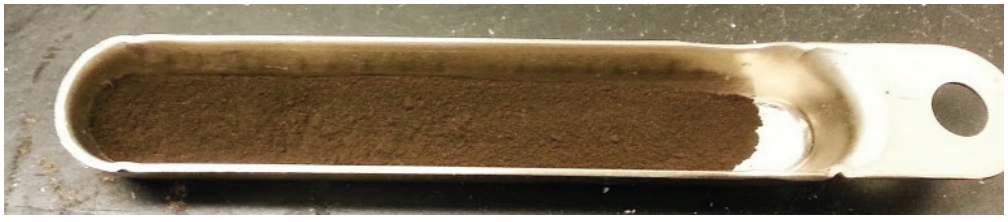

Figure 5.1. Fe_3O_4 before ammonolysis

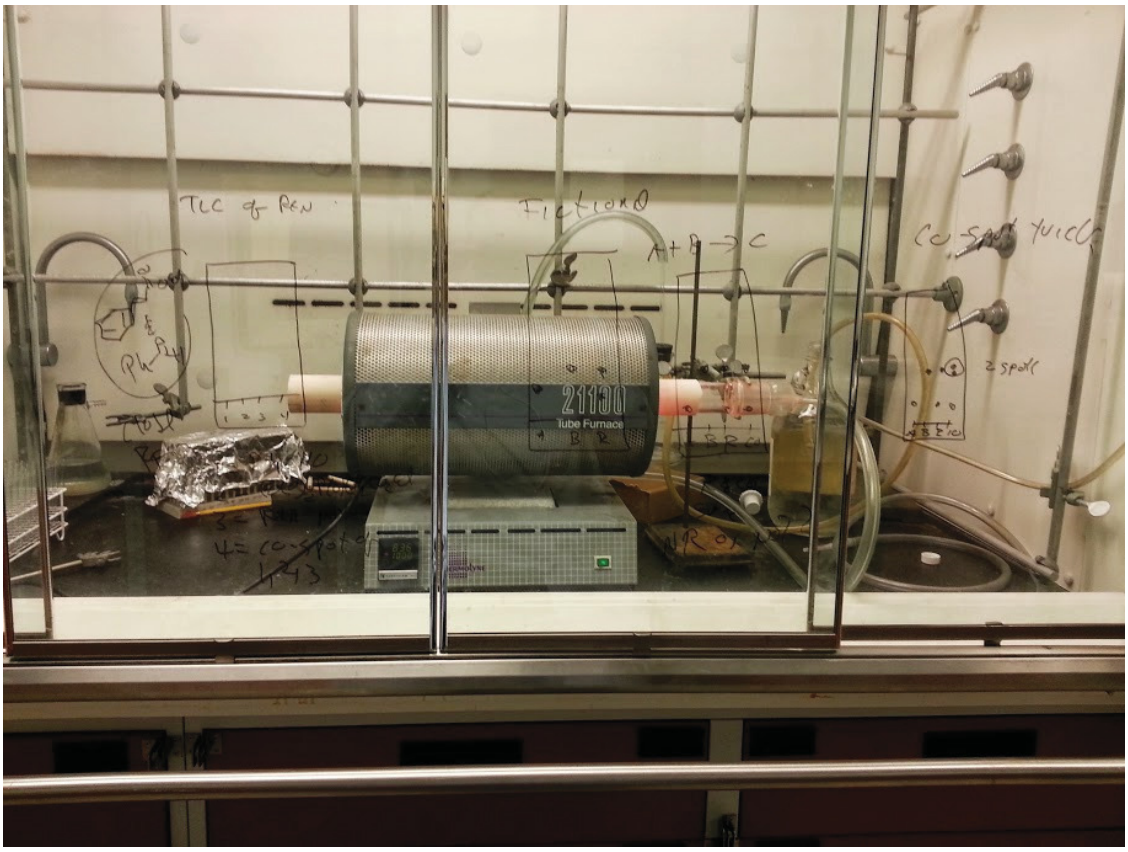

Figure 5.2. Ammonolysis setup

Before the furnace was started, a positive pressure of NH_3 was applied. This dynamic flow of NH_3 was measured by the bubble rate in an aqueous bubbler, where the ammonia gas would exit the system. This bubbler consisted of a solution of hydrochloric acid (HCl) that reacted with the excess NH_3 to produce ammonium chloride (NH_4Cl), which is disposed of easily. The furnace ran at 1000°C for approximately 12 hours, after which a reaction was noted to have taken place due to both an observed change in coloration (from brown to gray as seen in Figure 5.3) as well as a change in mass of the reactant material.

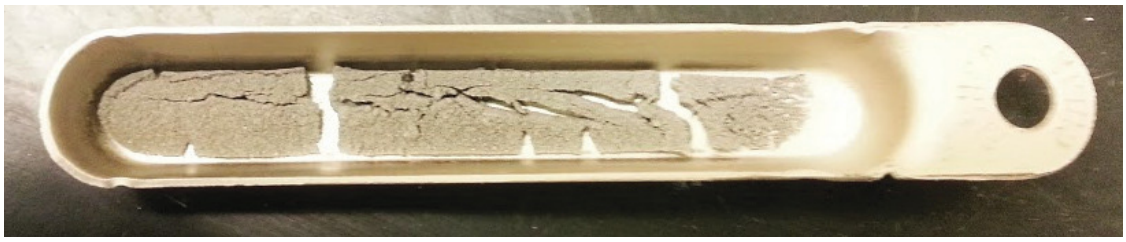

Figure 5.3. Fe_3O_4 after ammonolysis at 1000°C.

The sample lost 0.4628g during the course of the reaction, which indicated that the reaction had not taken place in the desired way, since, if it had, there would have been only a slight change in mass due only to partial displacement of oxygen by nitrogen. When the sample was examined using PXRD, it appeared to be a completely different product than targeted. As the powder pattern in Figure 5.4 shows, the final product appears to be an alloy of iron and nitrogen, $Fe_3N_{1.33}$, with oxygen having completely left the system. As Fe_3O_3N has never before been produced, it would not be in the database, but with all peaks accounted for in this situation, it seems that the reaction went completely in favor of this major product.

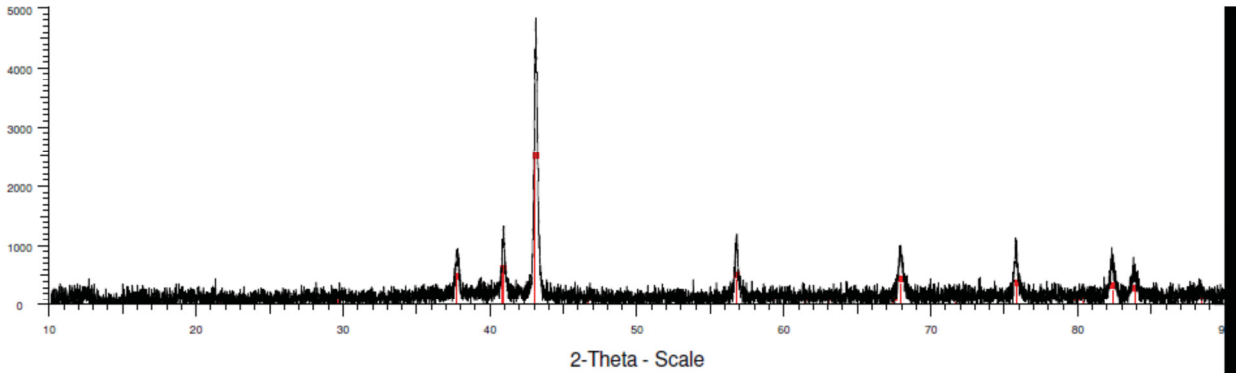

Figure 5.4. PXRD analysis of ammonolysis of Fe_3O_4

● Iron Nitride, 01-070-7408, $Fe_3N_{1.33}$, Hexagonal, a = 4.77150 Å, b = 4.77150 Å, c = 4.41500 Å [48].

As this synthesis was unsuccessful due to the near-complete reduction of iron, the experimental conditions needed to be changed. One of the possibilities included the amount of time for the reaction to occur. So, for the second attempt, 2.4876g (10.758 mmol) of Fe_3O_4 was placed in a nickel boat, with an identical setup to the first

ammonolysis attempt. The furnace was initially supposed to ramp up to 1000°C, but the furnace halted at 835°C due to malfunction, and the reaction was stopped after 3 hours and 8 minutes of time. Inspection of the resulting product showed a gradient of colors ranging from grey to blue to purple, as shown in Figure 5.5. After removing the sample from the silica tube, each of the different regions, blue, purple and grey, were examined using PXRD. With variations considered for height offsets, all three samples appeared to be very close approximations of each other, as shown in Figure 5.6, with the formula being $Fe_3N_{1.235}$, another alloy of iron and nitrogen. There were also two peaks at 21.5 and 24 degrees that are peaks from the wax used to affix the powder to the sample cup. Thus it appeared that even the shorter reaction time still led to the near-complete reduction of the iron.

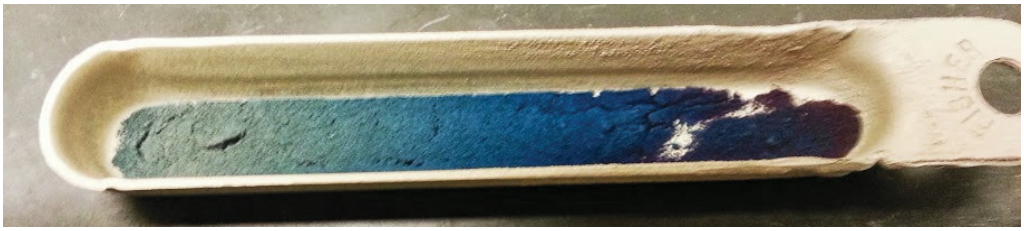

Figure 5.5 Sample of Fe_3O_4 after ammonolysis

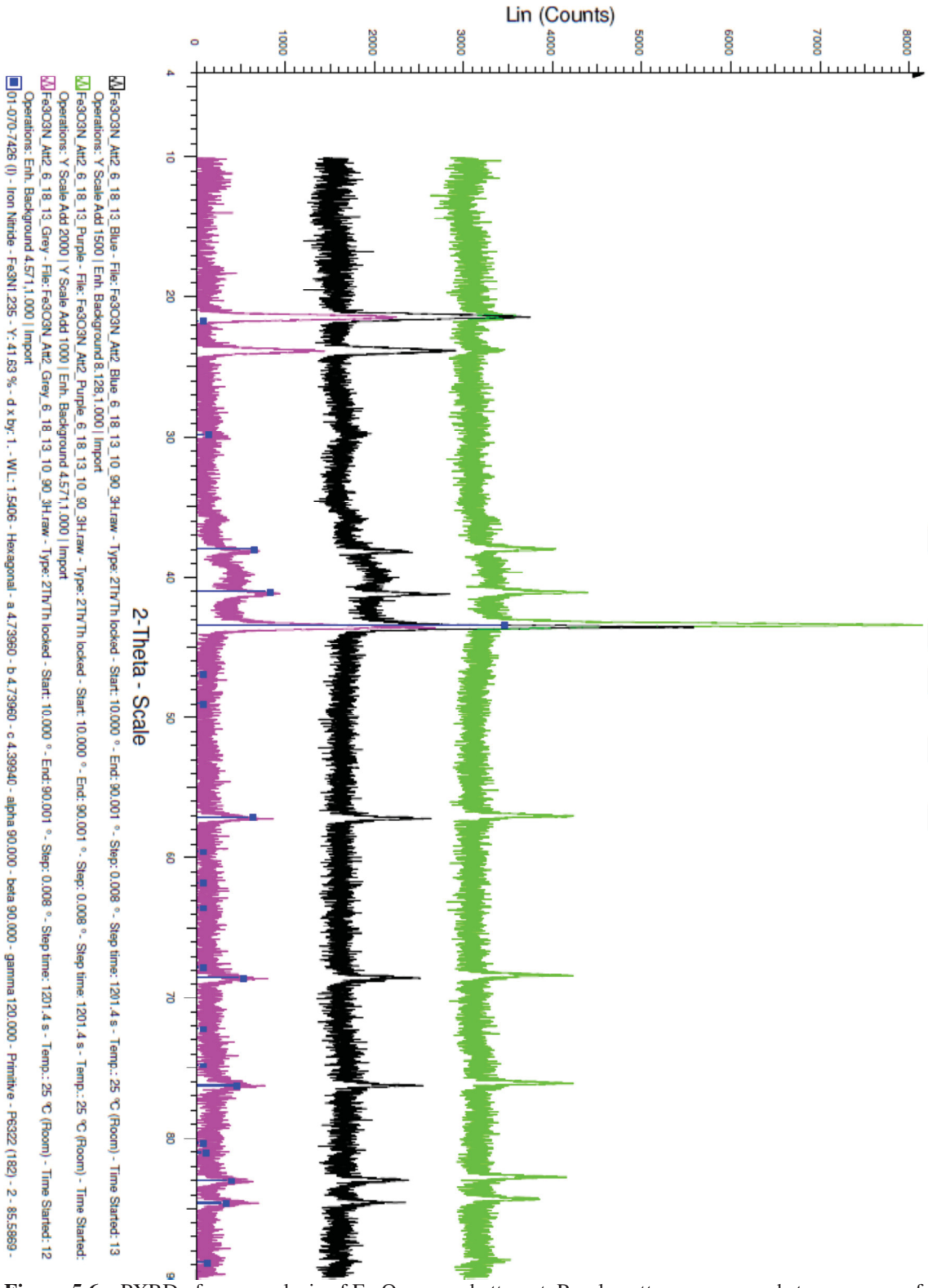

Figure 5.6. PXRD of ammonolysis of Fe_3O_4, second attempt. Purple pattern corresponds to grey area of sample shown in Figure 5.3, black pattern corresponds to blue area, and green pattern corresponds to purple area [48].

5.1.2 Fe_2O_3

Another possible route to form the iron oxynitride compound was using iron (III) oxide, Fe_2O_3, as seen in Figure 5.7. Using the ammonolysis setup, 3.3463g (20.955 mmol) of Fe_2O_3 was placed in the nickel boat with the reaction running for 3 hours and 30 minutes at 537.5°C. Afterwards, the sample was found to have changed color, as seen in Figure 5.8.

Figure 5.7 Fe_2O_3 in a nickel boat before ammonolysis

Figure 5.8 Fe_2O_3 after ammonolysis

Once PXRD was completed, two different phases of iron oxide, Fe_2O_3 and Fe_3O_4, along with an alloy of iron and nitrogen, Fe_3N, were found, as indicated by Figure 5.9. However, it should be noted that when the sample was initially removed from the furnace and exposed to air, it was observed that grains of material glowed bright red before fading to black. This reaction is postulated to be due to the instability of iron oxynitrides in air,, and is further discussed in the next section.

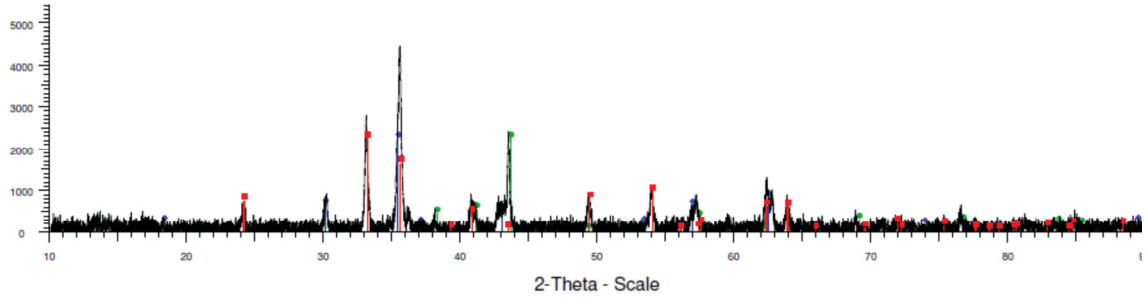

Figure 5.9 PXRD of Fe_2O_3 after ammonolysis, attempt 1.

- Hematite, 01-071-5088, Fe_2O_3, Rhombohedral, R-3c, a = 5.03850 Å, b = 5.03850 Å, c = 13.74000 Å, alpha = 90.000, gamma = 120.000 [49].
- Magnetite, 04-005-4319, Fe_3O_4, Cubic, Fd-3m, a = 8.39580 Å, alpha 90.000 [50].
- Iron Nitride, 04-007-3376, Fe_3N Hexagonal, P6322, a = 4.69960 Å, c = 4.38040 Å [51].

A second attempt of reacting Fe_2O_3 in NH_3 was performed , this time with a new setup to accommodate an atmosphere without air as seen in Figure 5.10. A glove bag was added to the fume hood so that after the completion of the reaction, the sample could be handled inside an atmosphere consisting of argon.

Figure 5.10 Setup used to react Fe_2O_3 with ammonia in an atmosphere without oxygen.

Thus 3.1091g (19.470 mmol) of Fe_2O_3 was placed in a nickel boat and reacted at 537.5°C for 3.5 hours. After the reaction was completed the entire tube was cooled in air with the ammonia replaced with argon via a T-junction. Once cooled, the tube was placed in the

glove bag, and the powder was combined with petroleum jelly to coat the particles against oxygen so that they could be analyzed via PXRD. The resulting diffraction pattern is shown in Figure 5.11, and indicates some differences relative to the powder pattern in Figure 5.9 taken from the Trial 1 sample exposed to air. First of all, there is little or no Fe_2O_3 phase evident in Figure 5.11 from the Trial 2 glove bag-protected sample, suggesting that the Fe_2O_3 observed in the Trial 1 PXRD pattern is not leftover starting material. Instead, since the reaction temperature, time & NH_3 flow conditions were identical for the two trials and the masses of the starting Fe_2O_3 reactant very similar, it is possible that the Fe_2O_3 observed only in the Trial 1 data is due to the decomposition of an oxynitride product in air.

This is further supported by a second, more subtle difference between the Trials 1 & 2 PXRD patterns, which is that all of the experimental peaks in Figure 5.11 matched to magnetite, are actually shifted slightly to the left relative to the known peaks from the database, whereas this is not the case in Figure 5.9 for the Fe_3O_4 peaks observed. This is the trend that would be expected if indeed N^{3-}, being larger in size relative to O^{2-}, were substituted for an O^{2-} ion in Fe_3O_4 to give the isostructural oxynitride, Fe_3O_3N. Based on this analysis, it would appear that an air-sensitive oxynitride phase of Fe_3O_3N was successfully prepared in both trials, and likely reacts in air according to reactions such as the following:

$$2Fe_3O_3N + O_2 \rightarrow 2Fe_3O_4 + N_2 \qquad \text{Equation (5.4)}$$

or

$$2Fe_3O_3N + 3H_2O \rightarrow 3Fe_2O_3 + 2NH_3 \qquad \text{Equation (5.5)}$$

Oxidation of oxynitrides is known to occur via similar reactions for ABO_2N compounds such as $LaTiO_2N$ [52]. Finally, it should be noted that both Trial 1 & 2 PXRD patterns show the presence of Fe_3N alloy-type phases. Based on the results from ammonolysis of Fe_3O_4 described earlier, this would likely have been the sole product observed for both trials if reaction times had been extended.

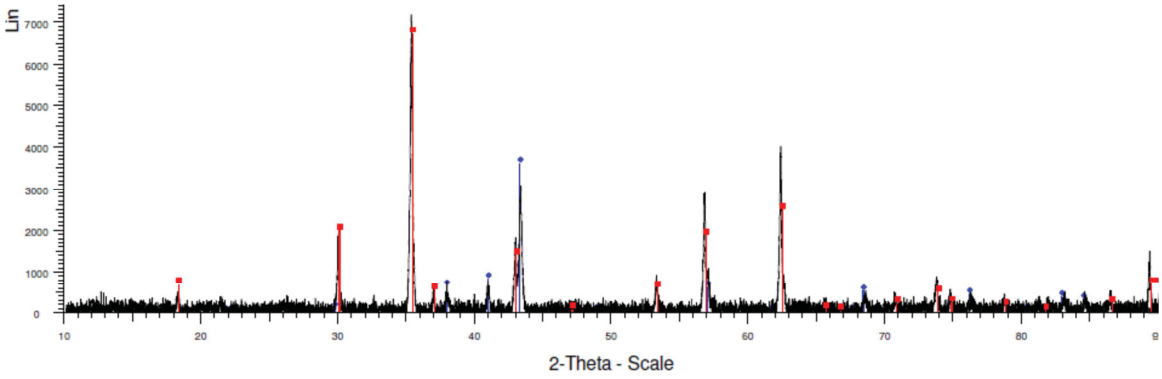

Figure 5.11 PXRD of Fe_2O_3 after reaction with ammonia, attempt 2

- Magnetite, 04-005-4319, Fe_3O_4, Cubic, Fd-3m, a = 8.39580 Å, alpha 90.000 [50].
- Iron Nitride, 01-070-7406, $Fe_3N_{1.239}$, Hexagonal, P6322 a = 4.74160 Å, c = 4.40080 Å [48].

5.1.3 Analysis

In the ammonolysis experiments described above targeting the preparation of the novel spinel oxynitride phase Fe_3O_3N; it was found that Fe3O4 is not a suitable precursor, while Fe2O3 appears to have worked to generate the desired product. The apparently successful reaction was run at relatively low temperature (just over 500º C) for a relatively short time (3.5 hrs.), and the final product was protected from air to avoid decomposition to iron oxides. Further analysis (e.g. neutron diffraction), would be required to verify the synthesis of Fe_3O_3N, however, if the data in Figure 5.11 is due to Fe_3O_3N as we propose, the compound is a cubic spinel isostructural with Fe3O4 as targeted. In the case of the Fe_3O_4 reaction, one of the iron atoms would have needed to be oxidized to create Fe_3O_3N, which in hindsight is not feasible using ammonia, a known reducing agent. For both sets of reactions, it was found that there was reduction of iron to FeN1+x phases, with complete reduction occurring in the case of Fe3O4 and partial reduction for the Fe2O3 reactions. The FeN_{1+x} compounds are known to be very stable and most likely any iron oxide heated in a stream of ammonia long enough will completely reduce to one of these closely related phases. In any case, work with Fe_3O_3N was not pursued further in this thesis, because it would not be practical to transform air sensitive material to obtain the final ceramic-metallic composites targeted.

5.2 Fe_2AlO_3N

Fe_2AlO_3N is a compound that has never been successfully synthesized before, but is desirable due to the stoichiometric ratio between Fe_2AlO_3N and Al_3O_3N, as shown in Equation 5.6.

$$Fe_2AlO_3N + (x+2)Al \rightarrow Al_3O_3N + FeAl_x \qquad \text{Equation (5.6)}$$

As Fe_2AlO_3N has also never been synthesized, the starting route was to sinter Fe_2O_3 and AlN as defined in Equation 5.7.

$$Fe_2O_3 + AlN \rightarrow Fe_2AlO_3N \qquad \text{Equation (5.7)}$$

5.2.1 Synthesis

A mass of 3.5821g (22.432 mmol) of Fe_2O_3 was combined with 0.9194g (22.431 mmol) of AlN, and the mixture was ball milled in a mixer for 20 minutes, and then uniaxially pressed into pellets using a steel die press. These pellets were then placed in an alumina boat and the boat placed inside a tube furnace and sintered at 1450°C for 36 hours under a constant positive pressure of N_2. The product, as seen in Figure 5.12, had a secondary reaction with the alumina crucible.

Figure 5.12. Sample of Fe_2O_3 and AlN sintered together for 36 hours at 1450°C.

One of the pellets was ground up via ball milling to prepare it for PXRD analysis. After analysis, the product was found to be a combination of $FeAl_2O_4$ ($Fe_{1.006}Al_{1.994}O_4$) and elemental iron, as shown in Figure 5.13. The actual reaction which possibly occurred is:

$$Fe_2O_3 + AlN \rightarrow ½\ FeAl_2O_4 + 1.5\ Fe + ½\ N_2 + ½\ O_2 \qquad \text{Equation (5.8)}$$

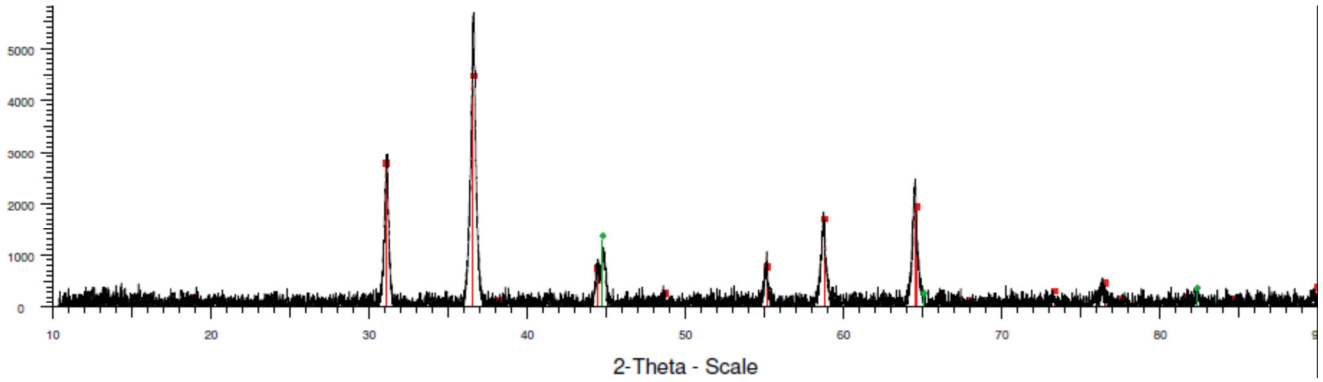

Figure 5.13. PXRD of Fe_2O_3 sintered with AlN.

- Iron Aluminum Oxide, 01-082-1580, $Fe_{1.006}Al_{1.994}O_4$, Cubic, Fd-3m, a = 8.15470 Å [53].
- Iron, 04-007-9753, Fe, Cubic, Im-3m, a = 2.86520 Å [54].

After examining the results of the first attempt, one of the possible reasons for failure involved the mixing time being too short. Longer mixing times would lead to a better coating of the Fe_2O_3 particles by the finer AlN particles. So, the mixing time was increased to 24 hours via ball milling. A mass of 3.5826g (22.435 mmol) Fe_2O_3 was mixed with 0.9194g (22.431 mmol) AlN, which, after ball milling, was uniaxially pressed into pellets using a steel die press. The same conditions as the previous trial (sintering at 1450°C for 36 hours under nitrogen gas) were used for this experiment, so as to best replicate the conditions and examine if the mixing time had any effect. The results can be seen in Figure 5.14.

Figure 5.14. Fe_2O_3 mixed with AlN and sintered for 36 hours at 1450°C

The two samples looked almost identical in terms of sample color. As in the first trial, the product had a secondary reaction with the alumina boat. The sample was examined via PXRD, and the results can be found in Figure 5.15.

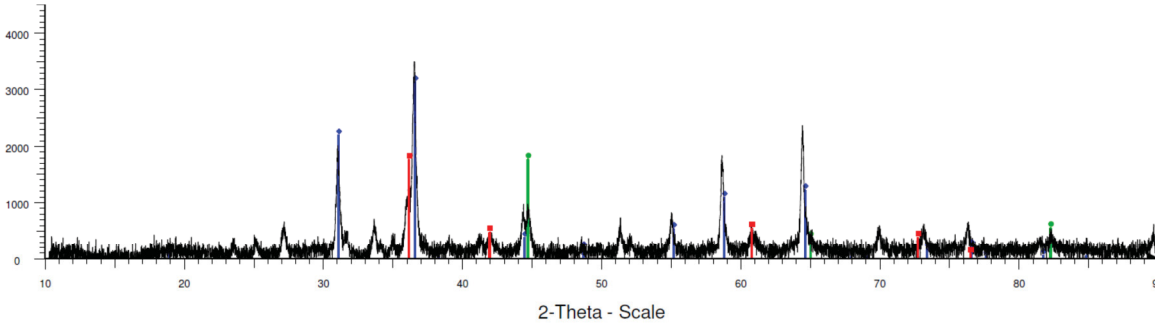

Figure 5.15. PXRD analysis of Fe_2O_3 mixed with AlN

- Iron Nitride, 04-003-1172, FeN Cubic, F-43m, a = 4.30700 Å [55].
- Iron Aluminum Oxide, 04-001-8940, $FeAl_2O_4$, Cubic, Fd-3d, a = 8.15000 Å [56].
- Iron, syn, 00-006-0696, Fe, Cubic, Im-3m, a = 2.86640 Å [57].

The products of this reaction were $FeAl_2O_4$, FeN, and elemental iron. Thus, increased time of ball milling, resulting in smaller particle sizes, evidently enhanced reactivity between the Fe_2O_3 and AlN reactants. Interestingly, from closer inspection of the PXRD pattern it can be seen that the $FeAl_2O_4$ experimental peaks are shifted slightly left relative to the database positions, again suggesting that some nitrogen may be present in the phase. However, this would be difficult to prove considering that the sample is not a pure phase, but is mixed with FeN.

5.2.2 Analysis:

As a single phase Fe-Al oxynitride phase was not prepared, this sample was not further investigated for transformation to composite material.

5.3 $SiAl_2O_2N_2$

SiO_2 is the most common system studied for RMP reactions, and when trying to incorporate oxynitrides into the ceramic phase of IPCs, a system analogous to SiO_2 would be a good place to start. $SiAl_2O_2N_2$, commonly called β-Sialon, would be a system that hopefully would act as an analog to SiO_2. Using the synthesis route from Tessier *et al.* [38], SiO_2 would be combined with AlN as shown in Equation 5.9.

$$SiO_2 + 2AlN \rightarrow SiAl_2O_2N_2 \qquad \text{Equation (5.9)}$$

For the first trial, 1.2567g (20.917 mmol) of SiO2 was mixed with 1.7433g (42.538 mmol) of AlN via ball milling for 24 hours. After ball milling, the powder was uniaxially pressed into pellets. In all, three pellets were pressed and placed into a nickel crucible one on top of the other such that the bottom pellet would serve as a sacrificial pellet in case of reaction with the crucible, one would be used for PXRD analysis, and third would be transformed in molten aluminum if the reaction was successful. The crucible was placed inside a steel tube in a tube furnace permitting dynamic flow of nitrogen gas. A positive pressure of nitrogen gas was applied, and the reaction was set to react via the route outlined by Tessier *et al.* [38]. This route involved ramping up at 10°C per minute until the reaction reached 1300°C, and then continuing to ramp up at 1.5°C per minute up to 1450°C. There was no dwell time listed in the paper, so one hour was used. At the end of the run, it was discovered that a hole developed in the tube, meaning that the reaction had been compromised such that any results, while still of note, would be tainted by not knowing how long the hole had been there, and if the nitrogen flow had continued through most of the reaction. The crucible had fused to the inside of the tube, but the pellets were still recovered. The PXRD of the recovered pellets is shown in Figure 5.16.

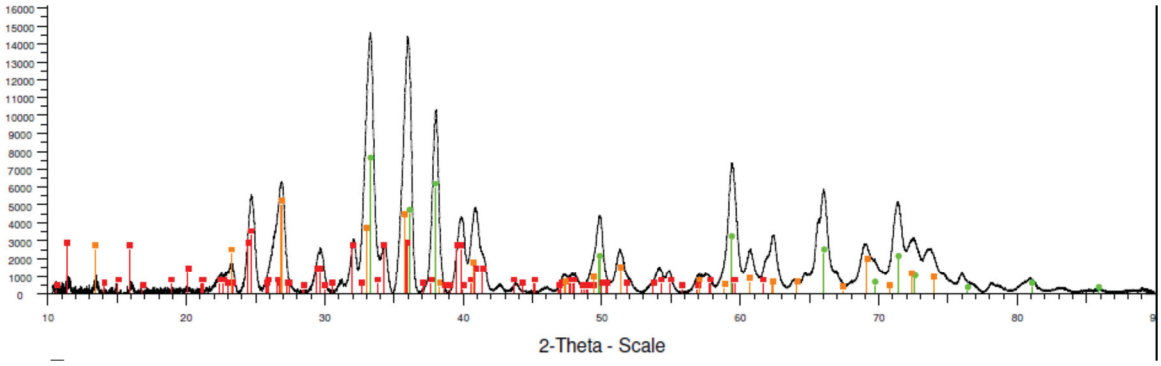

Figure 5.16. PXRD of β-Sialon sample from steel tube.

- Aluminum Nitride, 00-025-1133, AlN, Hexagonal, P63mc, a = 3.11140 Å, c = 4.97920 Å [58].
- Aluminum Silicon Oxide Nitride, 00-048-0637, $Al_{18}Si_{12}O_{39}N_8$, Triclinic - a = 9.68300 Å, b = 8.55200 Å, c = 11.21300 Å, alpha = 90.000, beta = 124.403, gamma = 98.480 [59].
- Aluminum Silicon Oxide Nitride, 00-036-1333, $Si_3Al_3O_3N_5$, Hexagonal, P63/m, a = 7.67810 Å, c = 2.97690 Å [60].

While the dominant phase was AlN, there were some silicon aluminum oxynitrides made in the process. The $Si_3Al_3O_3N_5$ doesn't have the same stoichiometric configuration as the β-Sialon, but the peak locations from P Tessier *et al.* [38] showed that these were identical peaks for the β-Sialon. This demonstrated that while this sample was tainted, it was possible to create the β-Sialon via this synthesis route.

So in a second trial, 1.6764g (27.903 mmol) of SiO_2 was mixed with 2.3249g (56.721 mmol) AlN for 24 hours via ball milling, and then the powder was uniaxially pressed into pellets and placed in an alumina boat. This trial however used an alumina rather than a steel tube, and the same experiment was performed. The same route was used to ramp to 1450°C, but this time the hold time was 48 hours. After the cycle completed, the pellets were pulled out, and the result can be seen in Figure 5.17.

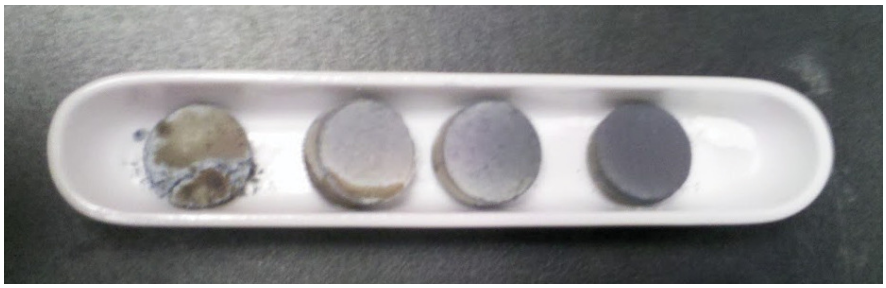

Figure 5.17. β-Sialon samples after sintering for 48 hours at 1450°C

The sample was then prepared for PXRD, and as shown in Figure 5.18, the results indicate a mixture of aluminum oxide and the silicon aluminum oxynitride as observed in the first trial. The Al_2O_3 is the dominant component with the rest being a mixture of the β-Sialon phase and two different crystalline forms of SiO_2.

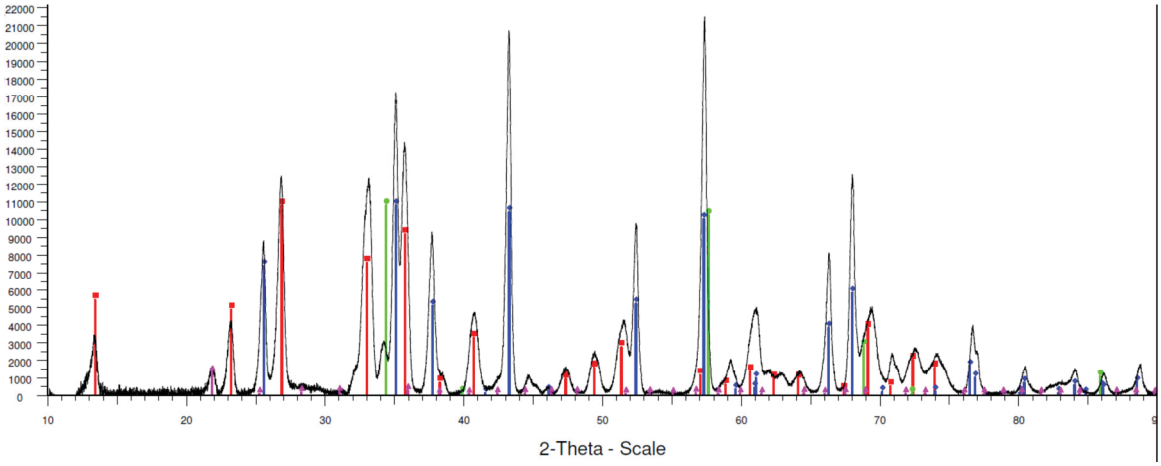

Figure 5.18. PXRD pattern of β-Sialon sample after sintering for 48 hours.

- Aluminum Silicon Oxide Nitride, 00-036-1333, $Si_3Al_3O_3N_5$, Hexagonal, P63/m, a = 7.67810 Å, c = 2.97690 Å [60].
- Aluminum Oxide, 04-004-2852, Al_2O_3, Rhombohedral, R-3c, a = 4.77012 Å, c = 13.04202 Å, alpha 90.000, gamma 120.000 [61].
- Silicon Oxide, 01-089-3609, SiO_2, Cubic, Fm-3m, a = 4.52000 Å [62].
- Cristobalite, syn, 01-082-0512, SiO_2, Tetragonal, P41212, a = 4.99700 Å, c = 7.07000 Å [63].

As the dominance of the Al_2O_3 in the product mixture was considered to be possibly due to the long dwell time of the reaction, such that the sialon phase decomposed into Al_2O_3 and SiO_2, and so the reaction was tried a third time with a shorter dwell time. For this run, 1.6761g (27.948 mmol) SiO_2 was combined with 2.3243g (56.707 mmol) AlN and prepared the exact same way as before. This time however, with the reaction conditions otherwise the same, the dwell time was shortened to 12 hours. During this dwell time, the reaction was paused at about 6 hours and one of the pellets was removed for PXRD analysis in order to determine the progress of the reaction. After the 12 hour cycle completed, another pellet was also taken for PXRD analysis. The resulting powder patterns for these samples can been seen in Figures 5.19 and 5.20, respectively.

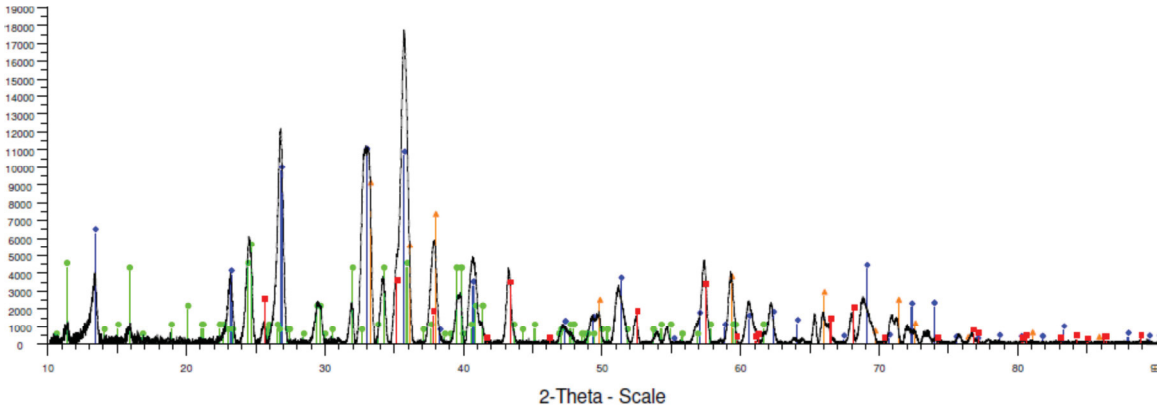

Figure 5.19. β-Sialon after 6 hours of sintering at 1450°C

- Aluminum Oxide, 04-004-2852, Al_2O_3, Rhombohedral, R-3c, a = 4.77012 Å, c = 13.04202 Å, alpha 90.000, gamma 120.000 [61].
- Silicon Aluminum Oxide Nitride, 01-079-0483, $Si_3Al_3O_3N_5$, Hexagonal, P63/m, a = 7.68050 Å, c = 2.97500 Å [64].
- Aluminum Silicon Oxide Nitride, 00-048-0637, $Al_{18}Si_{12}O_{39}N_8$, Triclinic, a = 9.68300 Å, b = 8.55200 Å, c = 11.21300 Å, alpha = 90.000, beta = 124.403, gamma = 98.480 [59].
- Aluminum Nitride, 00-025-1133, AlN, Hexagonal, P63mc, a = 3.11140 Å, c = 4.97920 Å [58].

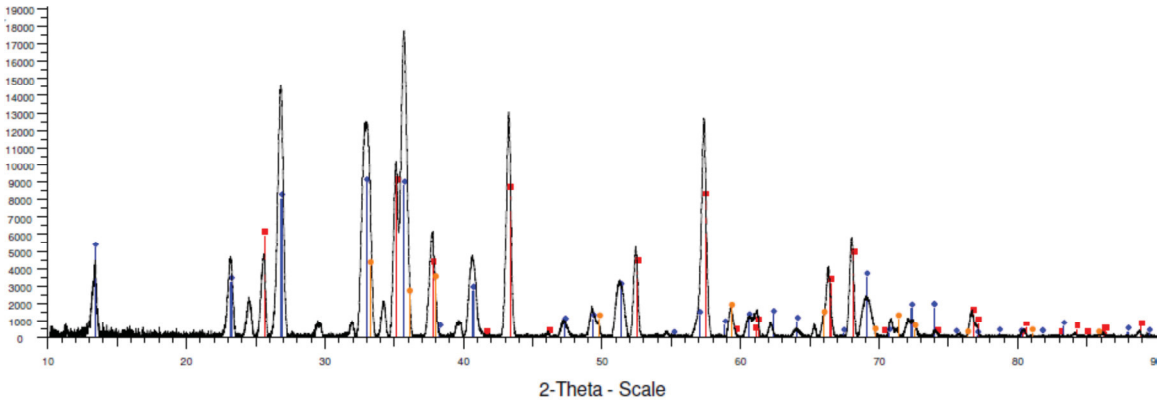

Figure 5.20. β-Sialon after 12 hours of sintering at 1450°C

- Corundum, 01-070-5679, Al_2O_3, Rhombohedral, R-3c, a = 4.75970 Å, c = 12.99350 Å [65].
- Silicon Aluminum Oxide Nitride, 01-079-0483, $Si_3Al_3O_3N_5$, Hexagonal, P63/m, a = 7.68050 Å, c = 2.97500 Å [64].
- Aluminum Nitride, 00-025-1133, AlN, Hexagonal, P63mc, a = 3.11140 Å, c = 4.97920 Å [58].

In the first pattern, the dominant phase is the Sialon as seen in the previous patterns, with other minor phases of Al_2O_3, AlN, and another silicon aluminum oxynitride, $Al_{19}Si_{12}O_{39}N_8$. The second pattern shows the disappearance of the second oxynitride phase, with a more dominant Al_2O_3 phase. This demonstrates that in both of the samples,

the Sialon is present, and so therefore this sample proved to be a viable sample for the transformation process. Afterwards, transformation of the 12 hour sample was performed as discussed in Chapter 4.1.1. Other samples generated using this synthesis were transformed via the process discussed in Chapter 4.1.2, and these results are discussed in Chapter 6.

5.4 $SrSi_2O_2N_2$

Another route to find an analog for SiO_2 was to synthesize $SrSi_2O_2N_2$ as outlined by O. Oeckler *et al*. [39]. This compound has a similar formula to the Sialon, but with the larger strontium atoms, it would theoretically leave larger channels for the aluminum to penetrate through as the strontium is released into the melt. Synthesizing the compound follows the route prescribed in Equation 5.10.

$$SrCO_3 + Si_3N_4 \rightarrow SrSi_2O_2N_2 + CO_2 \qquad \text{Equation (5.10)}$$

This reaction cannot be balanced as written, and in fact Oeckler *et al.* [39] reportedly used 0.7 mmol of $SrCO_3$ and 0.5 mmol Si_3N_4 to produce the targeted oxynitride along with impurities such as SrSiO3 and Si2N2O, as well as unspecified amorphous phases. The amounts used for the reaction by Oeckler *et al.* amounts to only milligrams of each reactant, which is too little for transformation, so the reaction was scaled up. Thus, 2.3760g (16.094 mmol) $SrCO_3$ was ball milled for twenty minutes with 1.6167g (11.525 mmol) Si_3N_4. It was then uniaxially pressed into pellets, and placed into a tube furnace. While under a constant positive pressure of nitrogen, the system was ramped up to 1250°C at 30°C/min, and once reached, by 55°C/hour to 1450°C. The system was then held at that temperature for 16 hours. Once complete the pellets were examined using PXRD, the results of which are found in Figure 5.21.

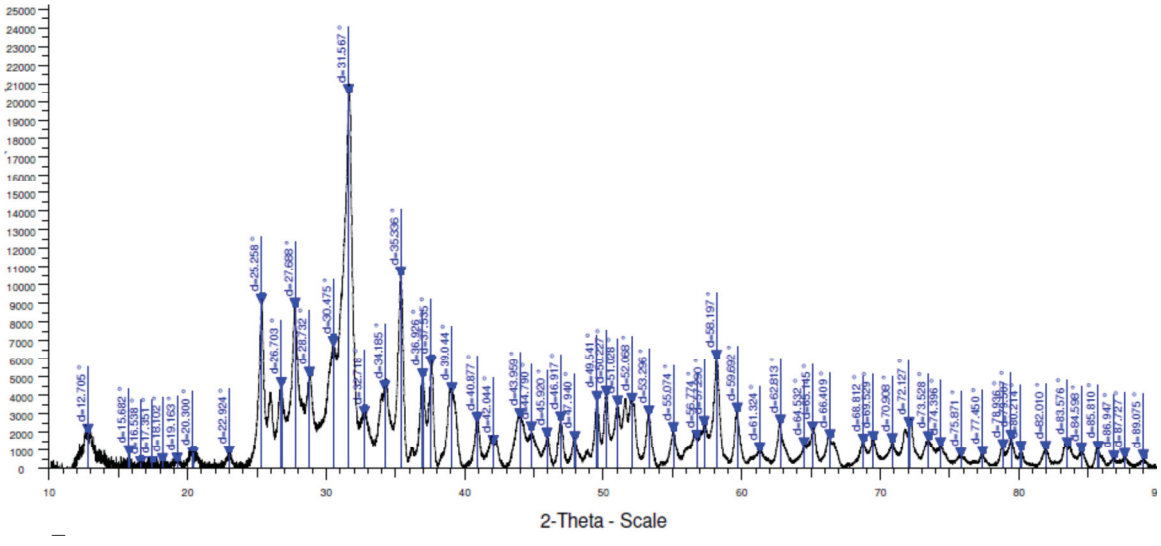

Figure 5.21. PXRD of SrSi2O2N2 sample

Now, the target compound was not in the database, and so, using the single crystal information (space group P1, a = 7.0802(2) Å, b = 7.2306(2) Å, c = 7.2554(2) Å, α = 88.767(3)°, β = 84.733(2)°, γ = 75.905(2)° and V = 358.73(2) $Å^3$, Z = 4) from O. Oeckler *et al* [39] theoretical d-spacings were generated. The calculated d-spacing information [66] was compared to the powder pattern shown in Figure 5.21 and found to be a match. The d-spacings are listed in Table 5.1.

Table 5.1 Comparison of calculated and experimental d-spacings [66]

Peak Number	Counts	Exp. d-spacing	Calculated d-spacing	Abs. value D_{exp}-D_{calc}	Phase	h	k	l
12.705	1811	6.96207	6.8395	0.12257	$SrSi_2O_2N_2$	1	0	0
15.682	626	5.64622	5.6262	0.02002	$SrSi_2O_2N_2$	1	1	0
19.163	191	4.62784	4.6044	0.02344	$SrSi_2O_2N_2$	1	1	1
20.300	469	4.37117	4.3925	0.02133	$SrSi_2O_2N_2$	1	-1	0
22.924	596	3.87632	3.8536	0.02272	$SrSi_2O_2N_2$	1	-1	1
25.258	8907	3.52313	3.6604	0.13727	$SrSi_2O_2N_2$	1	-1	-1
26.703	4356	3.33574	3.3190	0.01674	$SrSi_2O_2N_2$	1	2	1
27.688	8697	3.2192	3.2125	0.0067	$SrSi_2O_2N_2$	0	1	-2
28.732	4922	3.10458	3.0834	0.02118	$SrSi_2O_2N_2$	1	2	-1
30.475	6627	2.93093	2.9439	0.01297	$SrSi_2O_2N_2$	1	1	-2
31.567	20414	2.83194	2.8163	0.01564	$SrSi_2O_2N_2$	2	-1	0
32.718	2786	2.73494	2.7141	0.02084	$SrSi_2O_2N_2$	1	-1	-2
34.185	4183	2.62084	2.6190	0.00184	$SrSi_2O_2N_2$	1	-2	-1
35.336	10420	2.53808	2.5171	0.02098	$SrSi_2O_2N_2$	0	2	-2
36.926	4837	2.43233	2.4529	0.02057	$SrSi_2O_2N_2$	1	2	-2
37.535	5543	2.39424	2.3796	0.01464	$SrSi_2O_2N_2$	2	0	-2
39.044	4062	2.30513	2.3052	7E-05	$SrSi_2O_2N_2$	2	-1	2
40.877	2455	2.20586	2.1982	0.00766	$SrSi_2O_2N_2$	1	-2	-2
42.044	1205	2.1473	2.1455	0.0018	$SrSi_2O_2N_2$	2	-1	-2
43.959	2665	2.05813	2.0683	0.01017	$SrSi_2O_2N_2$	2	-2	-1
46.917	2495	1.93502	1.9268	0.00822	$SrSi_2O_2N_2$	2	-2	2
49.541	3598	1.8385	1.8302	0.0083	$SrSi_2O_2N_2$	2	-2	-2

After confirming that SrSi2O2N2 was indeed prepared, samples were transformed via the processes described in Chapter 4, sections 4.1.1. and 4.1.3, and the results are discussed in the next chapter.

Table 5.2 Summary of Precursor Reactions

Target Phase	Reaction Conditions	Results
Fe_3O_3N via Fe_3O_4	1000°C for 12 hours under NH_3	$Fe_3N_{1.33}$
Fe_3O_3N via Fe_3O_4	835°C for 3 hours 8 minutes under NH_3	$Fe_3N_{1.235}$
Fe_3O_3N via Fe_2O_3	537.5°C for 3.5 hours under NH_3	Fe_2O_3, Fe_3O_4, Fe_3N
Fe_3O_3N via Fe_2O_3	537.5°C for 3.5 hours under NH_3	Fe_3O_4, $Fe_3N_{1.239}$, possible oxynitride
Fe_2AlO_3N	1450°C for 36 hours under N_2	$Fe_{1.006}Al_{1.994}O_4$, Fe
Fe_2AlO_3N	1450°C for 36 hours under N_2	$FeAl_2O_4$, FeN, Fe
$SiAl_2O_2N_2$	10°C/min. to 1300°C, 1.5°C/min. to 1450°C for 1 hour under N_2	AlN, $Al_{18}Si_{12}O_{39}N_8$, $SiAl_2O_2N_2$
$SiAl_2O_2N_2$	10°C/min. to 1300°C, 1.5°C/min. to 1450°C for 48 hours under N_2	$SiAl_2O_2N_2$, Al_2O_3, SiO_2
$SiAl_2O_2N_2$	10°C/min. to 1300°C, 1.5°C/min. to 1450°C for 6 hours under N_2	Al_2O_3, $SiAl_2O_2N_2$, $Al_{18}Si_{12}O_{39}N_8$, AlN
$SiAl_2O_2N_2$	10°C/min. to 1300°C, 1.5°C/min. to 1450°C for 12 hours under N_2	Al_2O_3, $SiAl_2O_2N_2$, AlN
$SrSi_2O_2N_2$	30°C/min. to 1250°C, 55°C/min. to 1450°C for 16 hours under N_2	$SrSi_2O_2N_2$ and other impure phases

Chapter 6

Results

6.1 $SiAl_2O_2N_2$

6.1.1 Transformation via the TCON process

After the synthesis of the Sialon, it was transformed in molten aluminum at 1200°C. Once grinding was started, the composite fell apart, as shown in Figure 6.1. This revealed that the transformation reaction occurred only at the sample surface.

Figure 6.1. Sialon composite has fallen apart after grinding.

As indicated in Figures 6.2 and 6.3, PXRD analyses of each of the two pieces of the pellet shown in Figure 6.1 above verified that the edges and surfaces of the pellet is indeed AlN-Al_2O_3/Al composite, while the center of the pellet was verified to be unreacted Sialon.

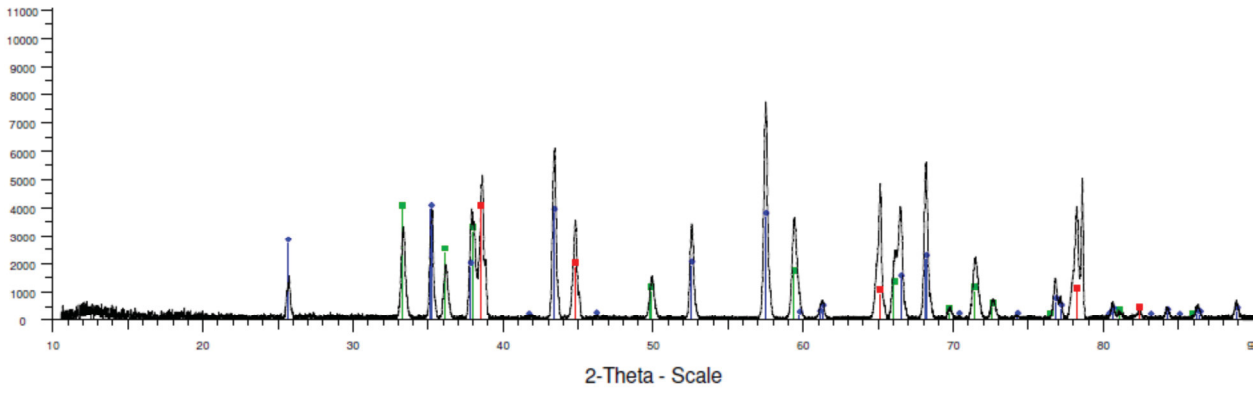

Figure 6.2. PXRD of top piece of pellet

- Aluminum Nitride, 00-025-1133, AlN, Hexagonal, P63mc, a = 3.11140 Å, c = 4.97920 Å [59].
- Aluminum, syn, 00-004-0787, Al, Cubic, Fm-3m, a = 4.04940 Å [67].

- Aluminum Oxide, 04-004-2852, Al_2O_3, Rhombohedral, R-3c, a = 4.77012 Å, c = 13.04202 Å, alpha 90.000, gamma 120.000 [62].

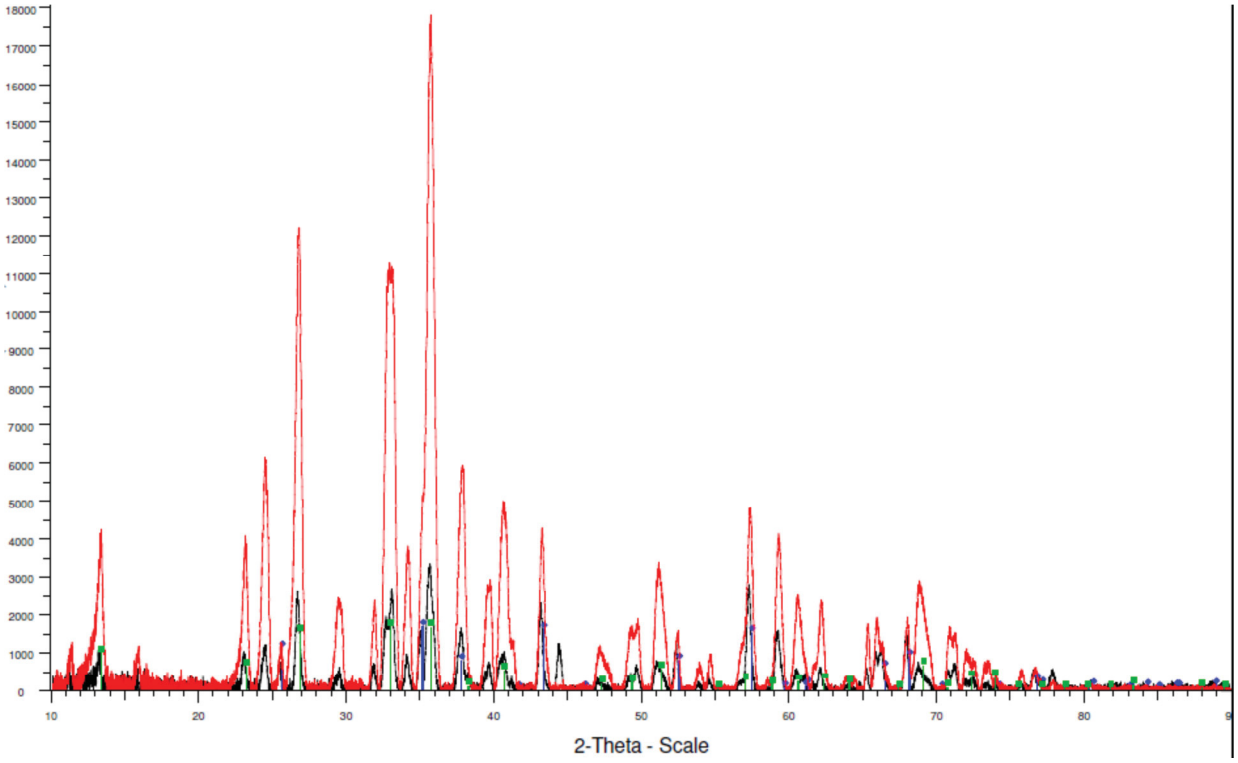

Figure 6.3. PXRD of the body of the pellet. The red outline represents the powder pattern for the starting materials as seen in Figure 5.21.

This showed that while some surface-level transformation did take place, the aluminum melt was not able to penetrate into the pellet. There are several reasons for this, with one of the reasons being due to thermodynamics. The reaction temperature may not have been high enough for the reaction to be able to take place. This was discussed in Chapter 1 in the examining of the difference between the wetting of SiO_2 and TiO_2. Due to the thermodynamic properties of the system, TiO_2 is not nearly as wettable as the SiO_2 system. This leads to only a minimal amount of transformation in a similar timeframe to a complete transformation of SiO2. It seems that a similar principle may be at work here. $SiAl_2O_2N_2$ shows a very minimal amount of transformation at a very similar level to that of TiO_2. This led to a minimal reaction, but as discussed in Chapter 1, this problem could be gotten around by increasing the temperature of the reaction so as to ensure that the higher temperature will drive the reaction.

Another reason that this reaction may not have worked is the density of the pellet. As discussed in Chapter 1, one of the criteria for transformation is that the specific volume of the produced ceramic phase must be smaller than that of the ceramic precursor material. When comparing the density of the two materials, it is noted that they are relatively close in value density (3.71g/cm^3 for AlON, and 3.146 g/cm^3 for Sialon). This, along with the fact that the reaction (given in Eq. 6.1) indicates 2 moles of Al3O3N are produced for every 3 moles of Sialon reacted means that their specific volumes are also similar.

$$3SiAl_2O_2N_2 + 4Al \rightarrow 2Al_3O_3N + 4AlN + 3Si \qquad \text{Equation (6.1)}$$

Recall that when an RMP reaction takes place, the reaction is able to propagate due to the formation of the ceramic phase of the composite having a smaller specific volume, which opens up gaps in the matrix allowing the penetration of aluminum. If the formed ceramic occupies about the same volume as the sacrificial ceramic phase, insufficient channels would be formed to allow adequate penetration of reactant molten metal into the pellet.

6.1.2 Transformation via Tube Furnace

Besides the lack of complete transformation of the sialon sample pellet, another problem noted early on is that it is thermodynamically impossible to achieve the desired aluminum oxynitride product at the maximum temperature of 1200°C that at which furnaces available for TCON reactions can operate. As indicated in the phase diagram shown in Figure 6.4 [60], the Al_3O_3N phase will form above about 1350°C, while at the actual reaction temperature of 1200 °C a mixed Al_2O_3-AlN product is expected.

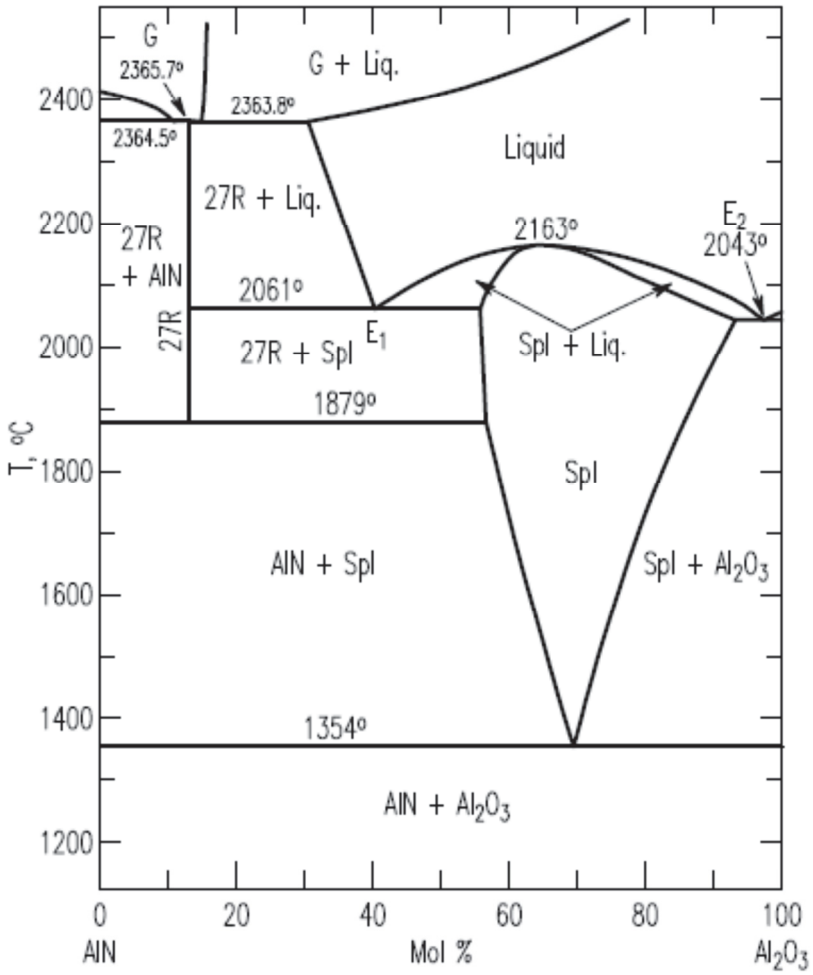

Figure 6.4 Phase diagram of AlN and Al_2O_3 [68].

To achieve the higher transformation temperature needed, the reaction was attempted using a tube furnace. The Sialon sacrificial pellet was placed in an alumina crucible and pure aluminum powder was added as the source of aluminum reactant. The reaction was held at 1450°C for 24 hours under dynamic N_2 flow. The first attempt failed due to the aluminum powder not properly achieving the molten state necessary for transformation, as shown in Figures 6.5 and 6.6.

Figure 6.5 Crucible after attempted transformation via tube furnace.

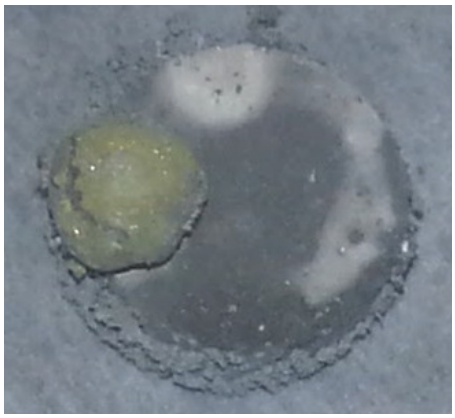

Figure 6.6 Pellet after attempted transformation via tube furnace.

This can be seen by the accumulation of feathery particles on the side of the crucible, and the state of the pellet. While some of the aluminum powder did appear to melt, as seen by the globule on the side of the pellet in Figure 6.5, the amount was insufficient to drive the reaction, especially considering that one of the conditions specified for the TCON process is that the reactant metal be available in excess. PXRD examination of the pellet clearly indicated that no reaction occurred. Thus, a second attempt was performed using a block of aluminum as the reactant source rather than powder, which perhaps had too much oxidized surface area to melt properly. . Another change for this trial was

increasing the reaction temperature to 1600°C for 24 hours, again under dynamic flow of N_2. The results were mixed in that a reaction took place, although not the one desired. The results of this trial are shown in Figures 6.7 and 6.8, first of all

Figure 6.7 Image of the crucible after reaction via tube furnace

Figure 6.8 Image of crystals formed on the top of the aluminum melt

Indicate that a secondary reaction took place between the crucible and the aluminum, possibly due to the elevated temperature used for the reaction, and as evident from the discoloration visible on the top half of the crucible. Once examined, the pellet showed no reaction at all with the block of aluminum, and the only noticeable change was the presence of yellowed crystals in the top of the aluminum melt that can be seen in Figure

6.8. These crystals were determined by single crystal X-ray diffraction to be aluminum carbide, Al_4C_3, which was due to the presence of impurities in the tube of the furnace most likely from unrelated experiments.

6.2 Transformation of $SrSi_2O_2N_2$ via the TCON Process

After the successful synthesis of the $SrSi_2O_2N_2$ precursor, a pellet was transformed in pure aluminum for 24 hours at 1200°C. The resulting pellet was ground and polished, and examination via optical microscopy revealed a composite with at least two phases, as seen in Figures 6.9, 6.10, and 6.11, which show the composite at 20x, 50x, and 100x respectively.

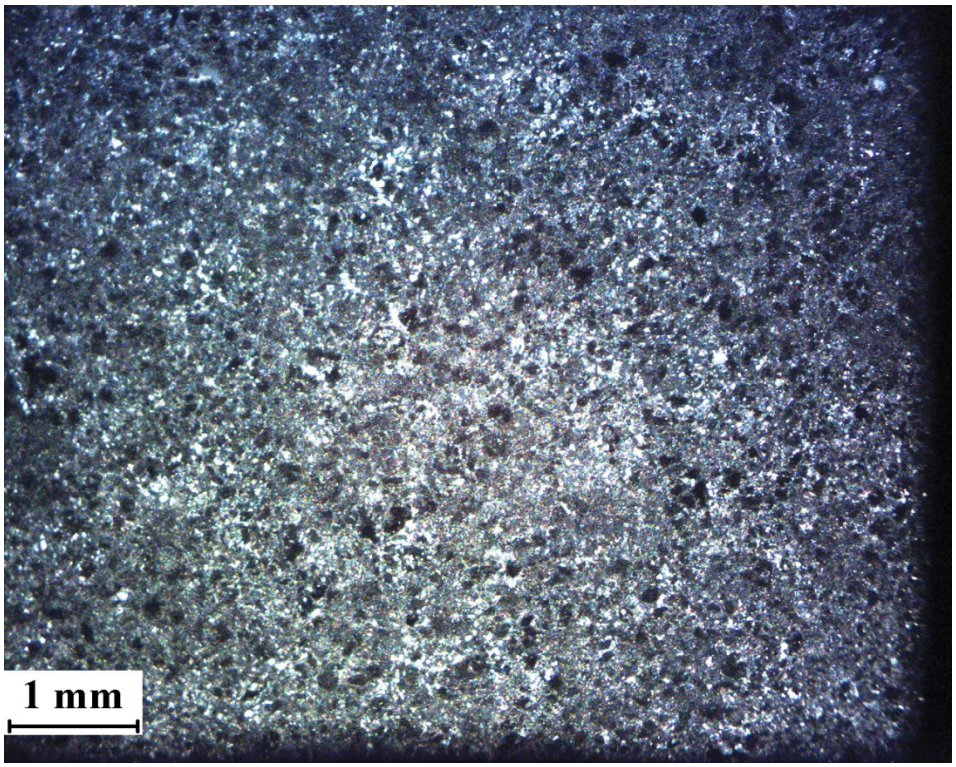

Figure 6.9 Optical microscopy image of composite from transformed $SrSi_2O_2N_2$ sample, taken at 20x magnification. Bright areas are aluminum, while the darker areas are ceramic components.

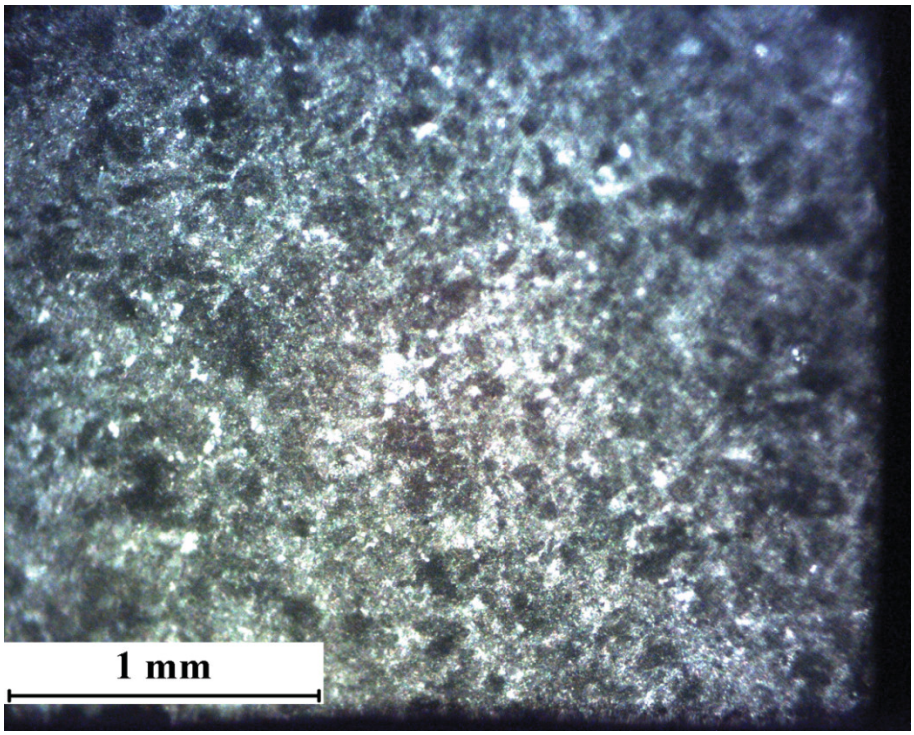

Figure 6.10 Optical microscopy image of composite from transformed $SrSi_2O_2N_2$ sample, taken at 50x - magnification. Bright areas are aluminum, while the darker areas are ceramic components

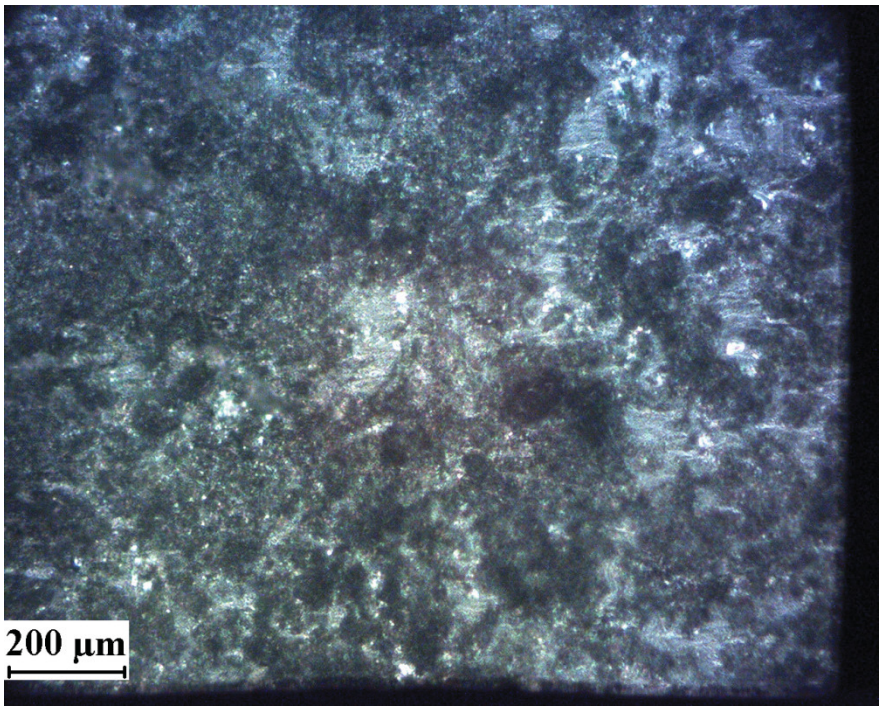

Figure 6.11 Optical microscopy image of composite from transformed $SrSi_2O_2N_2$ sample, taken at 100x magnification. Bright areas are aluminum, while the darker areas are ceramic components

The images show rather large grain sizes, some on the upper end of microscale, approaching milliscale. Having verified that this was, in fact, a composite, PXRD analysis was performed on the surface of the pellet to determine the phases present, and the results are given in Figure 6.12.

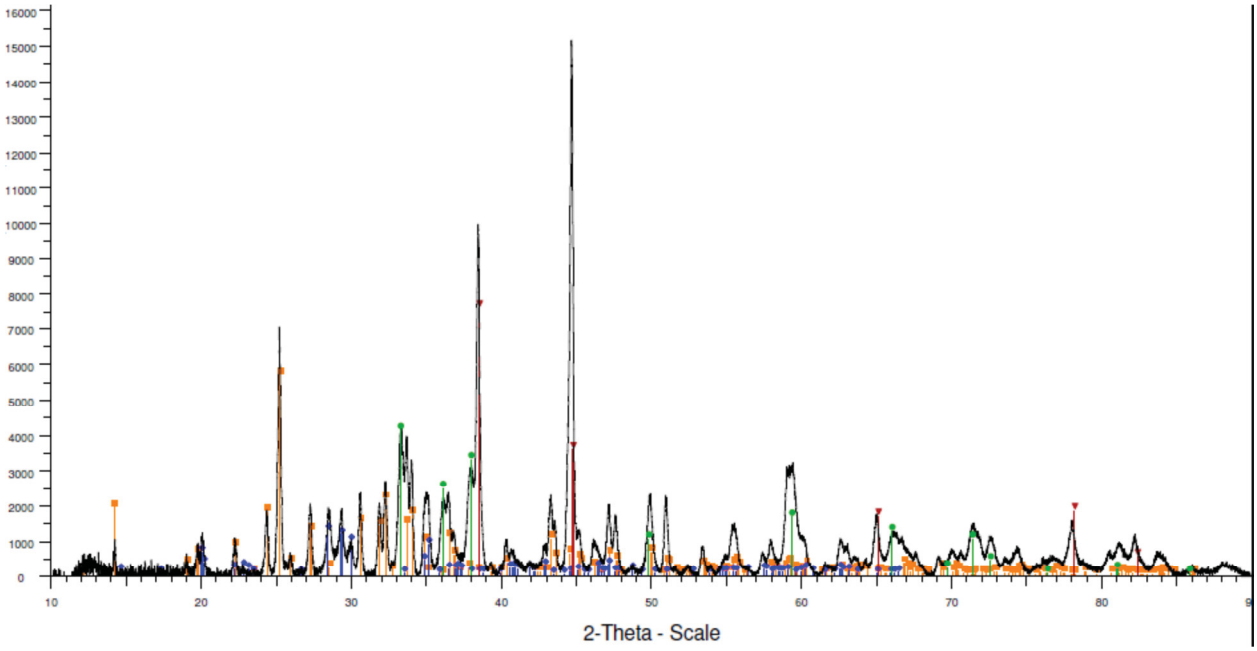

Figure 6.12 PXRD of surface of transformed $SrSi_2O_2N_2$ pellet.

- Strontium Aluminum Oxide, 04-007-5368, $SrAl_4O_7$, Monoclinic, C2/c, a = 13.03890 Å, b = 9.01130 Å, c = 5.53580 Å, alpha = 90.000, beta = 106.120 [67].
- Aluminum Nitride, 00-025-1133, AlN, Hexagonal, P63mc, a = 3.11140 Å, c = 4.97920 Å [59].
- Strontium Aluminum Oxide, 00-034-0379, $SrAl_2O_4$, Monoclinic, P*/*, a = 8.44240 Å, b = 8.82200 Å, c = 5.16070 Å, alpha = 90.000, beta = 93.415 [69].
- Aluminum, syn, 00-004-0787, Al, Cubic, Fm-3m, a = 4.04940 Å [70].

The PXRD pattern showed three major phases, $SrAl_4O_7$, AlN, and aluminum metal, with a minor phase containing $SrAl_2O_4$. None of these phases were the desired Al_3O_3N phase, and none of the phases were a cubic phase that would have been a match for the cubic aluminum phase of the composite. Nevertheless, transformation to composite did occur, and so further characterization was undertaken.

Having already prepared the sample via grinding and polishing, the sample was subjected to SEM and EDS analysis. The microstructure can be seen in the backscattered

image shown in Figure 6.13, where the darker regions represent the Al phase while the lighter regions are the ceramic components.

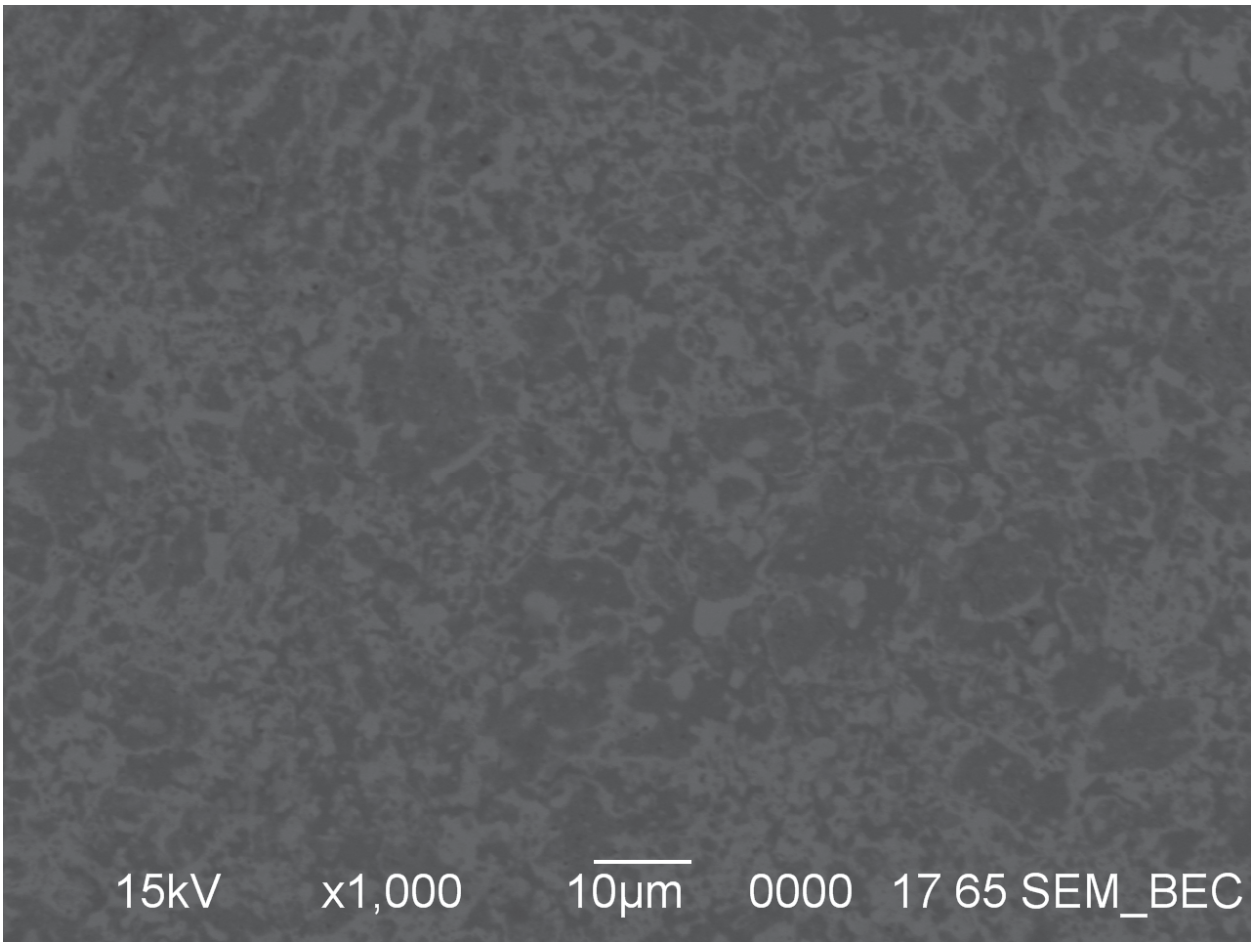

Figure 6.13 SEM (backscattered) image of the center of transformed $SrSi_2O_2N_2$ pellet at 2,000x. Though not optimal, the image does reveal the interpenetrating nature of the composite, with the darker regions the Al metallic phase and lighter regions ceramic component.

To further verify the compositions of the composite phases shown in Figure 6.12, EDS was performed. The results are shown in Figures 6.14 and 6.15 which correspond to the light and dark phases, respectively.

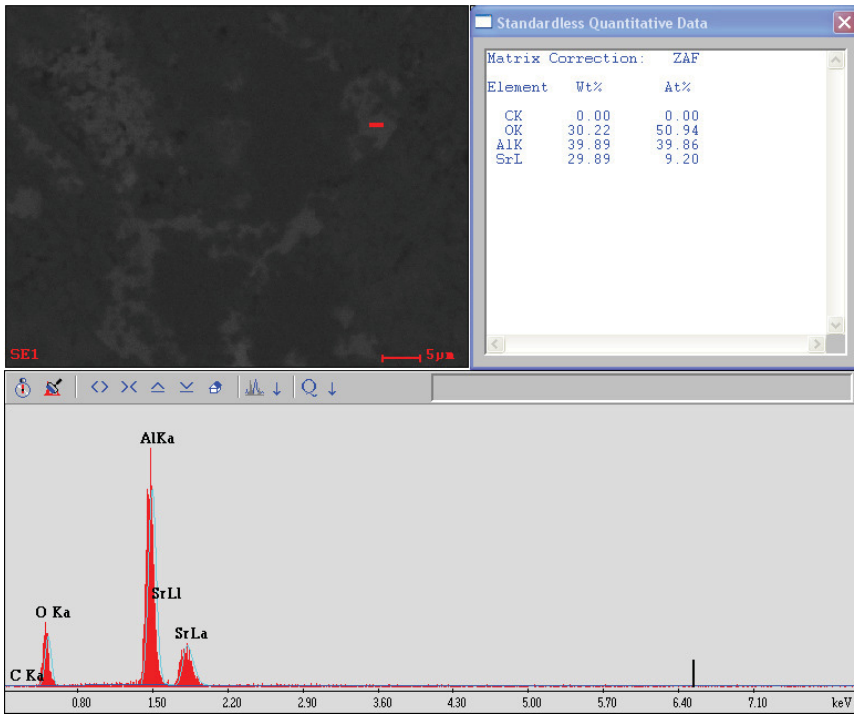

Figure 6.14 EDS analysis of a light phase region from $SrSi_2O_2N_2$, marked in red. Atomic percentages are listed in upper right quadrant.

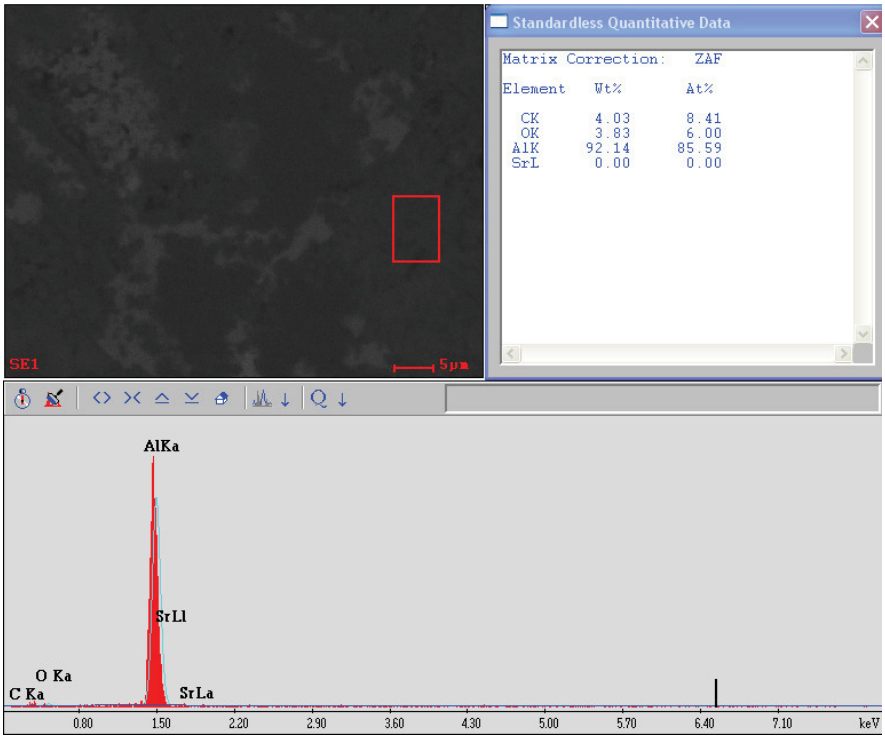

Figure 6.15 EDS analysis from a dark phase region from $SrSi_2O_2N_2$, marked in red. Atomic percentages are listed in upper right quadrant.

This analysis showed that the light phases indeed were consistent with of Sr-Al oxide phases, while the dark phases corresponded to aluminum.

One of the more interesting tools available using the EDS system is compositional image mapping, which assigns colors to each pixel in the image based on the element present at that location. This mapping was completed on an area, and helps to show that while some of these areas may be pure one phase or another, these phases could, on a smaller scale be strewn throughout one another. The first image, in Figure 6.16, shows the secondary electron image of the area, while the second image, in Figure 6.17 shows an image map recording from that area, with a color key.

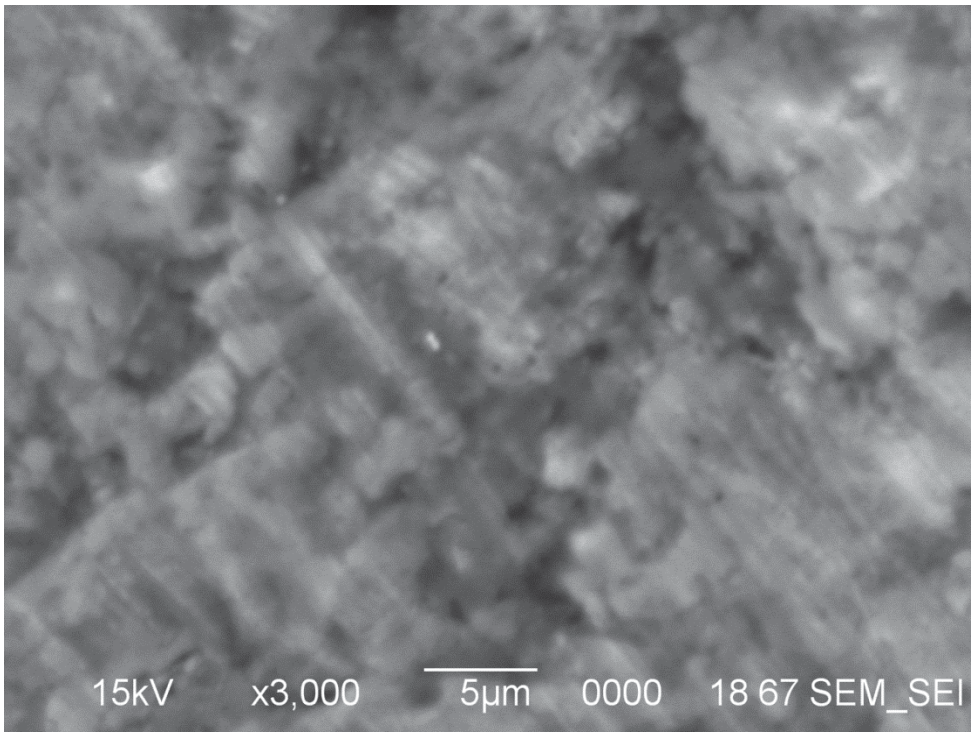

Figure 6.16 SEM Image of an area of $SrSi_2O_2N_2$ pellet.

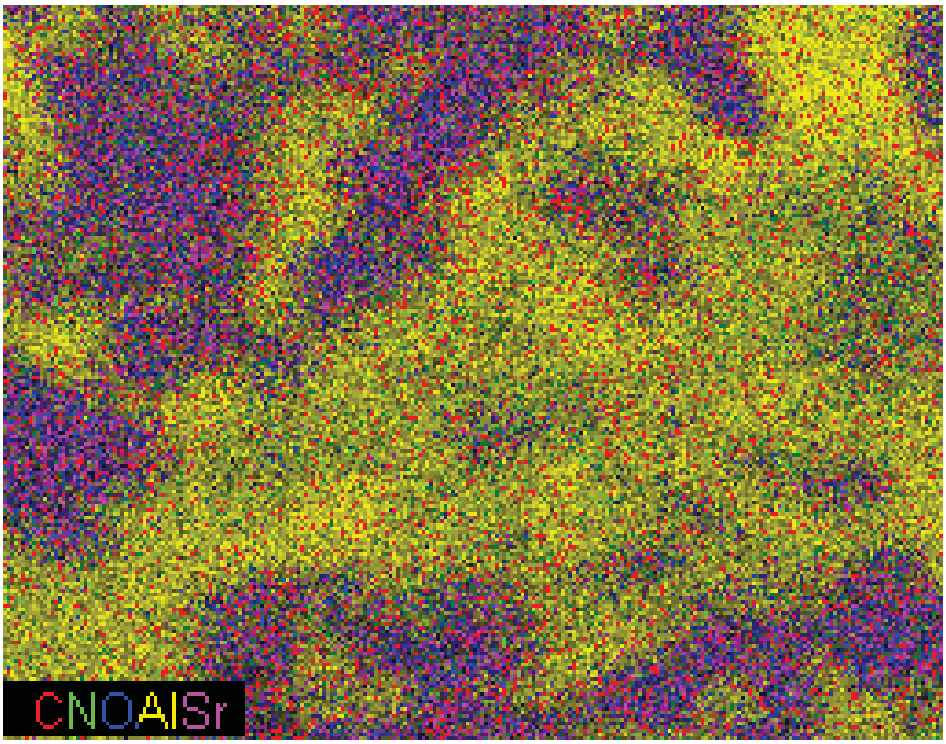

Figure 6.17 EDS mapping of same area as shown in SEM image in Figure 6.15.

In this image, the elements are represented by the following colors: carbon is represented by red, nitrogen is represented by green, oxygen is represented by blue, aluminum is represented by yellow, and strontium is represented by magenta. Note that the presence of carbon is due to SEM sample preparation. This mapping shows the relative locations of regions of the strontium aluminum oxide and aluminum metal phases, although a better indication of the elemental distributions is shown in the image maps below. The first map is of aluminum, shown in Figure 6.18.

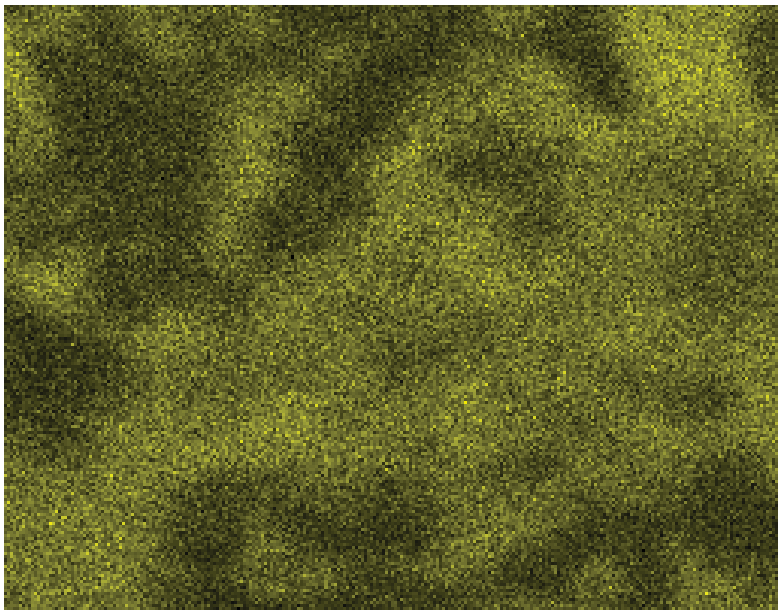

Figure 6.18 Elemental image map for aluminum from the same area shown in the SEM image in Figure 6.16.

This map, while showing that there are pockets where the aluminum is more prevalent, shows it is indeed present in all of the phases present, which was not apparent when all the maps were combined in Figure 6.17, due to the overwhelming presence of strontium and oxygen. The next series of maps, seen in Figures 6.19, 6.20 and 6.21, show the results for strontium, nitrogen, and oxygen, respectively.

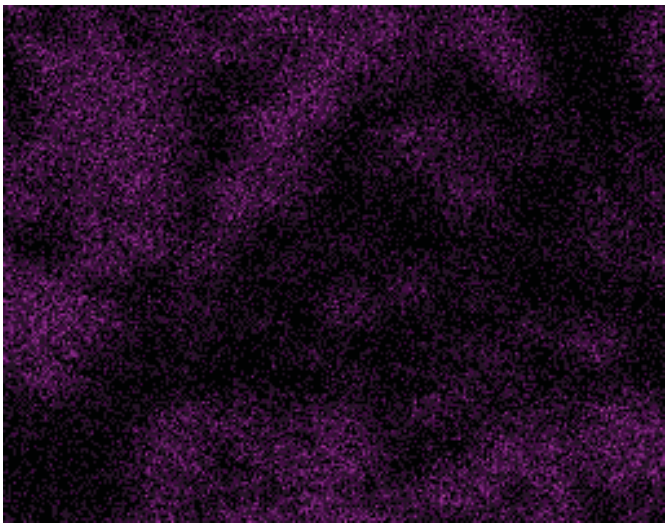

Figure 6.19 Elemental image map for strontium from the same area shown in the SEM image in Figure 6.16.

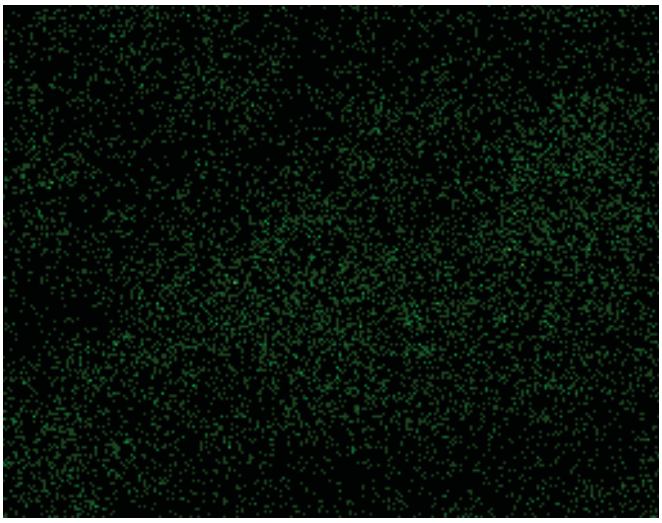

Figure 6.20 Elemental image map for nitrogen from the same area shown in the SEM image in Figure 6.16. Unlike the cases observed in the elemental maps acquired for strontium, aluminum, and oxygen, this map suggests that nitrogen is not more strongly correlated with one of the metallic or ceramic regions, but rather appears distributed throughout the composite.

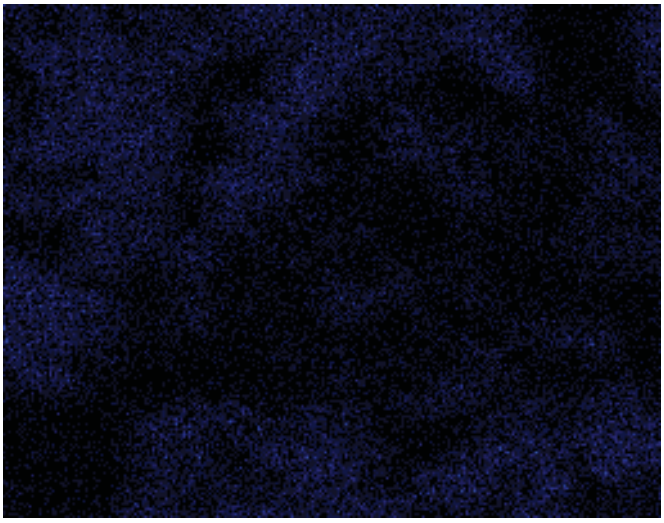

Figure 6.21 Elemental image map for oxygen from the same area shown in the SEM image in Figure 6.16.

The first and third maps show the same information as the aluminum map, only with the opposite phase correlations. The second map, showing nitrogen, shows no specific phase correlations, although there seems to be a slightly higher correlation with the areas with higher aluminum concentration. This would seem to indicate that the aluminum phases have concentrations of aluminum nitride, consistent with its presence in the PXRD pattern shown in Figure 6.12. As the elemental image map discussed here as well as the

SEM image and EDS data discussed above show that concentrated regions of AlN do not appear to present in the composite, it seems possible that AlN is instead dispersed throughout the composite as a nanophase. In order to verify that this is indeed the case, future studies would require analysis via high resolution transmission electron microscopy (TEM).

After the top of the pellet was investigated, the next step was to see if the pellet had completely or only partially transformed. So, the pellet was cut in half using a diamond saw, and appeared to have transformed completely from the picture shown in Figure 6.22.

Figure 6.22 `Photograph of transformed $SrSi_2O_2N_2$ pellet after being cut in half.

To confirm that this was in fact a complete transformation, the composite was examined using optical microscopy, and the resulting images at magnifications of 50x and 100x can be seen in Figures 6.23 and 6.24, respectively.

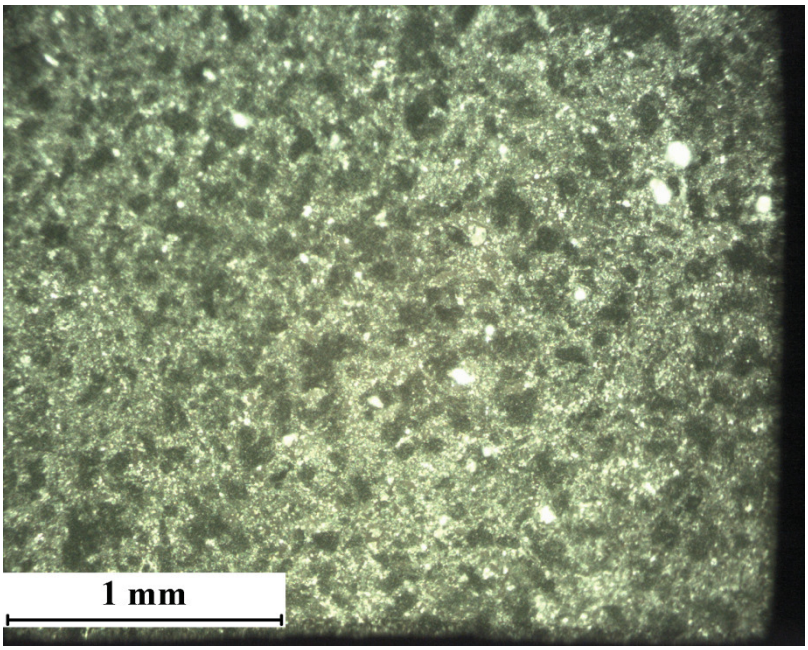

Figure 6.23 Optical microscope image of central region of transformed $SrSi_2O_2N_2$ pellet, clearly showing separate phase regions, 50x. The extremely bright spots are impurities from the diamond saw used to cut the sample.

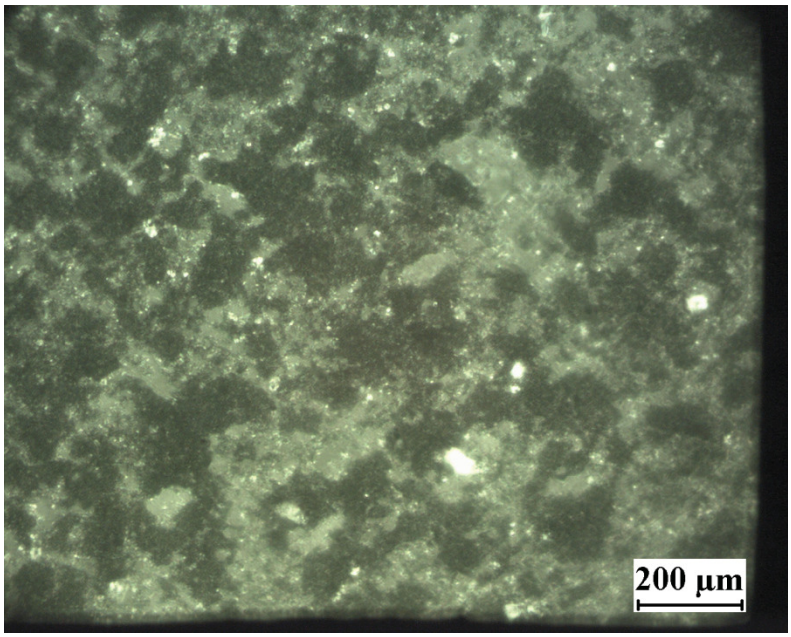

Figure 6.24 Optical microscope image of central region of transformed $SrSi_2O_2N_2$ pellet taken at 100x magnification. Separate phase regions of an interpenetrating phase composite are now more clearly evident. The extremely bright spots are impurities from the diamond saw used to cut the sample, while the light phase is aluminum and the dark phase is the ceramic components.

Both of these images indicate the presence of distinct phases, as expected from complete transformation of the $SrSi_2N_2O_2$ precursor. In particular, the higher magnification image in Figure 6.24 clearly shows that an interpenetrating phase composite has formed.

After confirming the complete transformation of the $SrSi_2O_2N_2$ pellet, the sample was ground down, polished, and analyzed via PXRD to verify the ceramic and metallic phases present. The pattern, shown in Figure 6.25, shows a much different composite composition than seen at the surface.

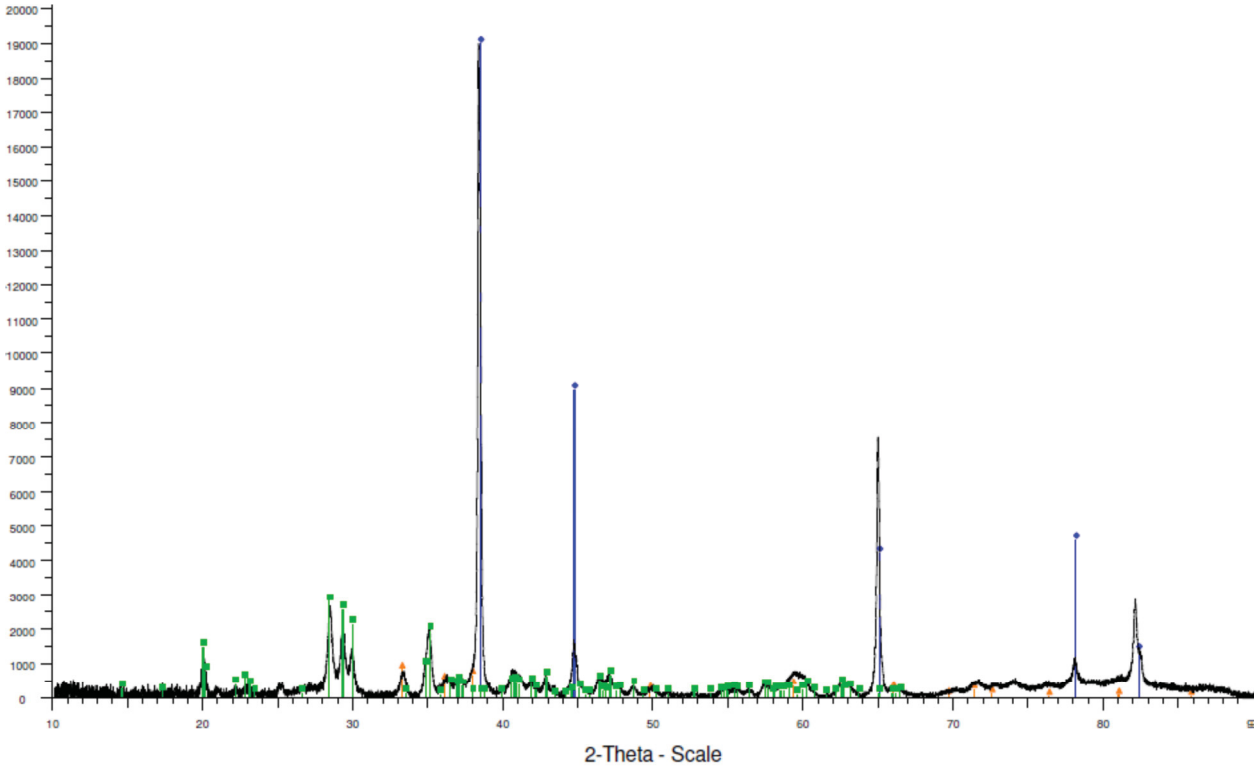

Figure 6.25 PXRD of interior of transformed $SrSi_2O_2N_2$ pellet after being cut.

- Strontium Aluminum Oxide, 00-034-0379, $SrAl_2O_4$, Monoclinic, P*/*, a = 8.44240, b = 8.82200, c = 5.16070, alpha = 90.000, beta = 93.415 [69].
- Aluminum, syn, 00-004-0787, Al, Cubic, Fm-3m, a = 4.04940 [67].
- Aluminum Nitride, 00-025-1133, AlN, Hexagonal, P63mc, a = 3.11140 Å, c = 4.97920 Å [58].

This shows that the interior of the pellet is mostly comprised of $SrAl_2O_4$ and aluminum, with a minor phase of aluminum nitride. No $SrAl_4O_7$ phase was observed, although this was the primary ceramic phase observed at the pellet surface (see Figure 6.12). This

difference in composition merited further analysis, using SEM, and resulting images can be seen in Figures 6.26 and 6.27.

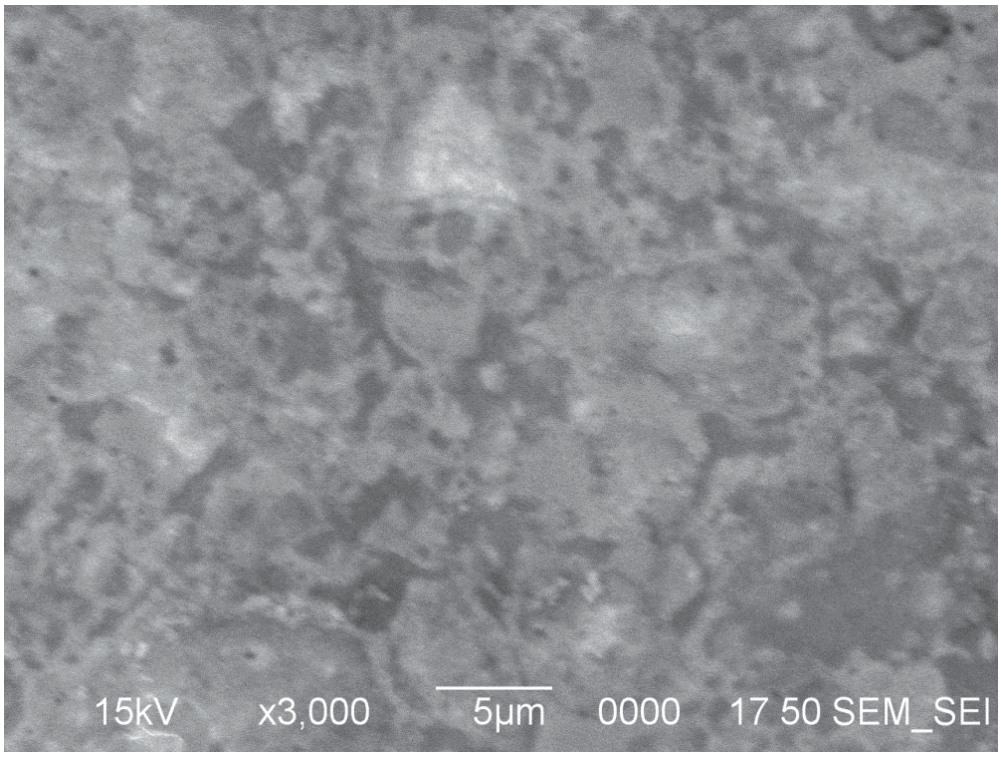

Figure 6.26 SEM micrograph of the central region of the transformed $SrSi_2O_2N_2$ pellet fracture at 3,000x. The darker regions are aluminum, while the lighter regions are the ceramic component.

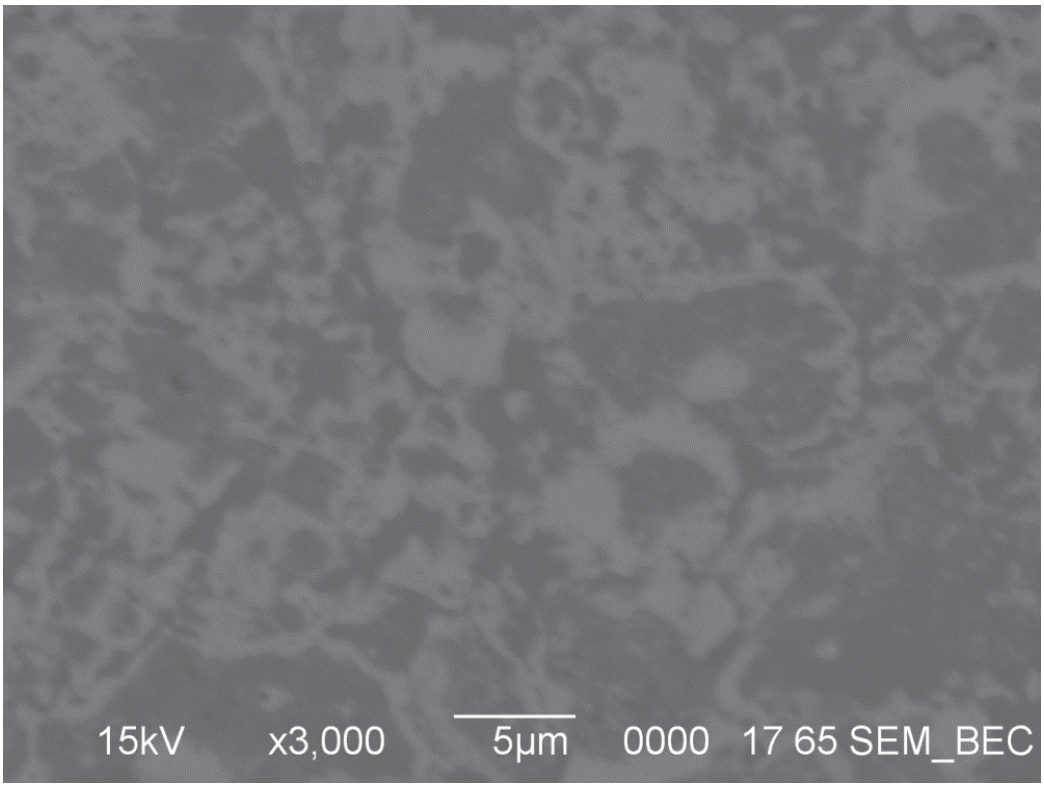

Figure 6.27 Backscattered SEM micrograph of the central region of the transformed $SrSi_2O_2N_2$ pellet, 3,000x. Light regions are the ceramic components, while the darker regions are aluminum.

These images further verify that this composite is a co-continuous throughout, with distinct ceramic and metallic phase regions. The lighter areas in the backscattered image theoretically correlate to $SrAl_2O_4$, as this was the main ceramic phases observed on the PXRD pattern above, while the darker areas correlate to aluminum metal. To confirm these phases, EDS was performed, the results of which can be seen in Figures 6.28 and 6.29.

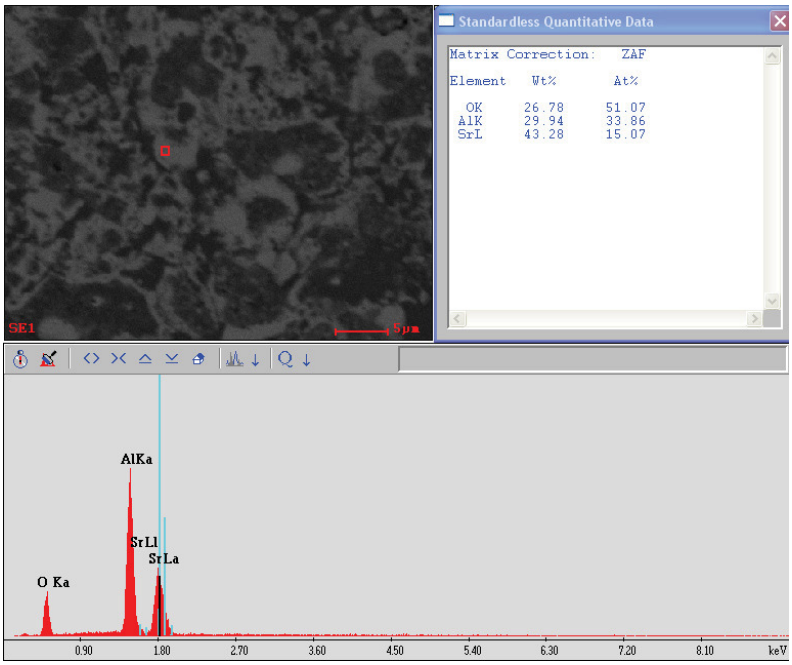

Figure 6.28 EDS of lighter phase region, marked in red, from image of transformed $SrSi_2O_2N_2$ sample shown in Figure 6.27

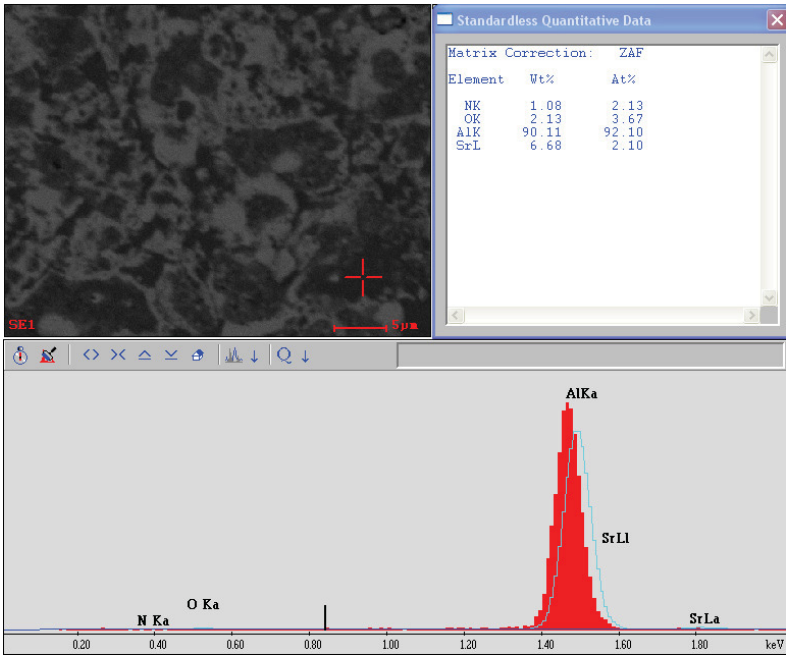

Figure 6.29 EDS of darker phase region, marked in red, from image of transformed $SrSi_2O_2N_2$ sample shown in Figure 6.27

The lighter areas appear to correspond to the $SrAl_2O_4$, though according to the data at this point the stoichiometric formula would be $SrAl_{2.2}O_{3.4}$. Also, according to the EDS data,

the dark phase again correlates to aluminum, but again has some impurities in the matrix. The effect observed on the surface with impurities in the matrix of both the light and dark phases seems to be consistent throughout the entire composite.

There is a stark difference between the composition of the areas directly on the surface of the pellet and the interior of the pellet, with the surface having a primary ceramic phase of $SrAl_4O_7$ while the interior is comprised mostly of a $SrAl_2O_4$ ceramic phase. As no Al_2O_3 was detected in the sample, it does not appear that $SrAl_4O_7$ decomposed to $SrAl_2O_4$ and Al_2O_3 in the pellet center, as might be first suspected. It should be noted here that even producing the $SrAl_2O_4$ phase directly at the pellet interior would require more oxygen than could be provided by a pure $SrSi_2O_2N_2$ precursor phase. Thus the $SrSi_2O_2N_2$ starting material must have contained an impurity, most likely (amorphous) SiO_2, so that a possible transformation reaction at the pellet interior could be:

$$SrSi_2O_2N_2 + \underline{SiO_2} + (4+x)Al \rightarrow SrAl_2O_4 + 2AlN + xAl + 3Si \qquad \text{Equation (6.2)}$$

Lack of detection of Si in the PXRD pattern would mean that most of the Si could have diffused into the bath during transformation. Regarding the formation of the $SrAl_4O_7$ phase at the pellet surface, this would require even more oxygen than needed to produce $SrAl_2O_4$. It is possible that upon removing the pellet from the reaction bath, surface Al oxidized to form Al_2O_3, which then reacted with $SrAl_2O_4$ to form the observed $SrAl_4O_7$ phase. Alternatively, Al_2O_3 could have been present in the molten Al bath such that reaction occurred during transformation.

Although the transformation of $SrSi_2O_2N_2$ did yield the desired composite containing the Al_3O_3N spinel-like oxynitrde ceramic phase, the experiment was a success in that complete transformation to an IPC occurred. Furthermore, this represents a new route being found for the incorporation of the ceramic phases of $SrAl_2O_4$ and $SrAl_4O_7$, which is the first time these phases have been incorporated into an IPC to our knowledge. Although these phases are monoclinic rather than cubic, it is worth investigating the mechanical properties of these composites in future work. Comparison to related composites with cubic spinel-aluminum interfaces prepared in work stemming from this

project could provide a test of the hypothesis stated herein that a cubic-cubic interface would provide more tightly bonded grains, and thus a stronger bulk composite.

Chapter 7
Conclusions and Future Work

7.1 Oxynitride Synthesis

One of the limiting factors in this thesis was the successful synthesis of some of the targeted oxynitrides. In the future, a possible inroad would be to use oxynitrides that can be purchased or more easily synthesized. An example of this would be the difference between the synthesis of the Sialon and the strontium silicon oxynitride. The Sialon took months of preparation and trial and error to successfully synthesize, but even when synthesized the system was not pure Sialon. On the other hand the strontium silicon oxynitride was successfully synthesized on the first attempt with any impurities being extremely minor phases. Though neither road was particularly successful in is project in forming a composite containing the desired Al_3O_3N phase, the strontium silicon oxynitride occupied much less time in the research path than did the Sialon, just due to the ease of synthesis. This is an important factor in a project such as this, in which potential commercialization with an active industrial partner is a consideration.

As for the oxynitrides of general composition $M_xAl_{3-x}O_3N$ ($0 < x < 3$), these compounds hold value - as long as they can be synthesized -, since they theoretically permit stoichiometric reaction with excess Al to form the desired Al_3O_3N-Al composite. This is because reaction requires only displacement of the M^{3+} in $M_xAl_{3-x}O_3N$ to give Al_3O_3N. As discussed in Chapter 5, Fe_3O_3N was possibly synthesized via an ammonolysis route in this study, although the phase appears to be air sensitive and so is not feasible for further transformation to composite in this study. Nevertheless, it would be interesting from a basic research perspective to verify the synthesis of this novel compound in future work. Preparation of Fe_2AlO_3N was not successful, instead leading to preferential formation of (possibly nitrogenated) $FeAl_2O_4$. In future work, related compositions containing metals such as Mn or Nd could be investigated towards the continuing goal of discovering a novel precursor that transforms to yield a stoichiometric Al_3O_3N-Al composite.

7.2 Transformation via the TCON Process

The transformation process is an experimental process that has been found to be very successful for the alumina/aluminum system. Although the $SrSi_2O_2N_2$ phase did successfully transform to an interpenetrating phase composite, as noted in Chapter 6, Sr-Al oxides were formed as the ceramic components rather than the desired aluminum oxynitride phase. A key reason for this is due to the temperature limits of the kilns used for laboratory transformations, which can attain a temperature of only about 1250°C, and even then it is not for nearly as long as the system would be stable at 1200°C. This is a problem because, as was seen in Figure 6.1, the aluminum oxynitride is only formed at temperatures above 1350°C, and even then, it is much more easily obtainable at temperatures above 1400-1450°C [68].

Thus, even if ceramics such as the Sialon or the strontium silicon oxynitride were to react under the TCON conditions, they would not be able to form the appropriate aluminum oxynitride phase. Attempts to perform the transformation reaction in laboratory furnaces (as opposed to kilns) capable of achieving temperatures up to 1700°C were not successful, and future work should investigate methods to perfect this technique. For example, such methods must ideally allow the sample to be preheated and introduced into a bath of excess molten Al, but without exposing the metal bath to air. The procedure should be first verified by studying transformation of SiO_2 in pure Al, and comparing the results to standard TCON composites. Further verification that an Al_3O_3N-Al composite can be formed using a laboratory tube or box furnace could justify purchase of a higher temperature kiln for future investigations.

References

1. Liu, W. and Köster, U. (1996). Criteria for Formation of Interpenetrating Oxide/metal-composites by Immersing Sacrificial Preforms in Molten Metals, Scripta Materialia, vol. 35(1), pp. 35-40.
2. Clarke, David R. (1992). Interpenetrating Phase Composites. Journal of American Ceramic Society, vol. 75(4), pp. 739-759.
3. Hemrick, J.C., Hu, M.Z., Peters, K.M. and Hetzel, B. (2010). Nano-Scale Interpenetrating Phase Composites (IPC's) for Industrial and Vehicle Application. (ORNL/TM-2010/80) Oak Ridge, TN.
4. Marchi, S.C., Kouzeli, M., Rao, R., Lewis, J.A. and Dunand, J.A. (2003). Alumina–Aluminum Interpenetrating-Phase Composites with Three-Dimensional Periodic Architecture. Scripta Materialia. Vol. 49, pp. 861-866.
5. Yurcho, A. (2010) Microstructural Investigation of Al/Al-Fe Alloy-Al2O3 Interpenetrating Phase Composites Produced by Reactive Metal Penetration. Master's Thesis, Youngstown State University, OH, U.S.A.
6. George, H. (1955). Manufacture of Articles from Substances Containing Silica. U.S. Patent No. 2,702,750.
7. Breslin, M.C. (1993). Process for Preparing Ceramic-Metal Composite Bodies. U.S. Patent No. 5,214,011.
8. Breslin, M.C., Ringnalda, J., Xu, L., Fuller, M., Seeger, J., Daehn, G.S., Otani, T. and Fraser, H.L. (1995). Processing, Microstructure and Properties of Co-Continuous Alumina-Aluminum Composites, Materials Science & Engineering. vol. A195, pp. 113-119.
9. Mas-Guindal, M.J., Benko, E. and Rodriguez, M.A. (2008). Nanostructured Metastable cermets of Ti-Al2O3 through Activated SHS Reaction. Journal of Alloys and Compounds. vol. 454, pp. 352-358.
10. Fahrenholtz, W.G., Ewsuk, K.G., Loehman, R.E. and Tomsia, A.P. (1996). Formation of Structural Intermetallics by Reactive Metal Penetration of Ti and Ni Oxides and Aluminates. Metallurgical and Materials Transactions A. vol. 27A, pp. 2100-2104.
11. Avraham, S. and Kaplan, W.D. (2005). Reactive Wetting of Rutile by Liquid Aluminum. Journal of Materials Science. vol. 40, pp. 1093-1100.

12. Sobczak, N., Stobierski, L., Radziwill, W., Ksiazek, M. and Warmezuk, M. (2004). Wettability and Interfacial Reactions in Al/TiO2. Surface and Interface Analysis. vol. 36, pp.1067-1070.
13. Chidambaram, P.R., Edwards, G.R. and Olson, D.L. (1992). A Thermodynamic Criterion to Predict Wettability at Metal-Alumina Interfaces. Metallurgical Transactions B. vol. 23B, pp. 215-222.
14. Surface & Coatings Technology 203 (2009) 941–951.
15. Sobczak, N., Wojewoda, J., Morgiel, J. and Nowak, R. (2010). Reactivity of Molten Aluminum with Polycrystalline ZnO Substrate. Journal of Materials Science. vol. 45, pp. 4291-4298.
16. Sobczak, N. (2006). Interaction between Molten Aluminum and Oxides. Solidification Processing of Metal Matrix Composites – Rohatgi Honorary Symposium. pp. 133-146.
17. Sobczak, N., Ksiazek, M., Radziwill, W., Warmuzek, M., Nowak, R. and Kudyba, A. (2003). Odlewnictwo – Nauka I Praktyka. vol. 3, pp. 3.
18. Sobczak, N., Stobierski, L., Radziwill, W., Ksiazek, M. and Warmuzek, M. (2004). Surface and Interface Analysis. vol. 36, pp. 1067.
19. Peters, K.M. and Hetzel, B. (2011). Private communication regarding the TCON process. Fireline Inc., Youngstown, OH.
20. Wagner, T. (2009). Synthesis, Characterization, and Applications of Mixed-Anion Inorganic Materials. Youngstown, OH.
21. Peters, K.M., Cravens, R.M., and Hemrick J.G. (2009). Advance Ceramic Composites for Improved Thermal Management in Molten Aluminum Applications. Energy Technology Perspectives: Conservation, Carbon Dioxide Reduction, and Production from Alternate Sources – Proceedings of Symposia held during TMS 2009 Annual Meeting and Exhibition, pp. 241-248.
22. Paul, R. (2007). Microstructural and Chemical Characterization of Interpenetrating Phase Composites as Unique Refractory Materials Produced Via Reactive Metal Penetration. Master's Thesis, Youngstown State University, OH, U.S.A.

23. Myers, K. (2011). Investigation of Novel Precursor Routes for Incorporation of Titanium Alloys and Nano-Sized Features into Ceramic-Metallic Composites Formed via the TCON Process. Master's Thesis, Youngstown State University, OH, U.S.A.
24. Lee M. Goldman et al. ALON® Optical Ceramic Transparencies for Sensor and Armor Applications, Surmet.
25. M. Moro, K.M. Peters, B.P. Hetzel, M. Zeller, T.R. Wagner, and V.C. Solomon, "Crystallographic investigations of microscopic ceramic and metallic phases in an Al-based interpenetrated phase composite", Microscopy & Microanalysis 18 (Suppl 2), 2012, 1930-1931.
26. Journal of the European Ceramic Society 5 (1989) 143-154.
27. http://www.surmet.com/docs/Product_sheet_ALON.pdf
28. R.E. Loehman and K. Ewsuk, "Synthesis of Al2O3-Al Composites by Reactive Metal Penetration", Journal of American Ceramic Society, 79(1), 27-32 (1996).
29. W.G. Fahrenholtz, K. Ewsuk, R.E. Loehman, and A.P. Tomsia, "Synthesis and Processing of Al2O3/Al Composites by In Situ Reaction of Aluminum and Mullite", In-Situ Reactions for Synthesis of Composites, Ceramics, and Intermetallics, pp. 99-109, ed. by E.V. Barrera et al., The Minerals, Metals, and Materials Society, Warrendale, PA, 1995.
30. Chem. Mater. 1991, 3, 242-252.
31. J. Phys. Chem. B 2004, 108, 12027-12031.
32. Ind. Eng. Chem. Res. 2005, 44, 2469-2476.
33. J. Phys. Chem. B 1997, 101, 9433-3435.
34. S. Rovner, "21st Century Armor", Chemical and Engineering News, 48-53, July 27, 2009.
35. F.C. Sahin, H. E. Kanbur, and B. Apk, "Preparation of AlON Ceramics via Reactive Spark Plasma Sintering", J. Eur. Ceramic Soc., 32, 925-929 (2012).
36. J.J. Swab, J.C. LaSalvia, G.A. Gilde, P.J. Patel, and M.J. Motyka, "Transparent Armor Ceramics: AlON and Spinel" 23rd Annual Conf. on Composites, Advanced Ceramics, Materials and Structures: B: Ceramic Eng. & Science Proceedings, 20(4), 79-84 (1999).

37. M. Basista and W. Weglewski, “Modeling of damage and fracture in ceramic-matrix composites”, Journal of Theoretical and Applied Mechanics, 44, 455-484 (2006).
38. Journal of Alloys and Compounds, 2005, 391, 225-227.
39. Solid State Sciences. 9, 2007, 205-212.
40. Bruker AXS. (2001). D8 Advanced X-ray Diffractometer User’s Manuel: Vol II. Karlsruhe, Germany: Bruker AXS GmbH.
41. Pecharsky, V.K. and Zavalij, P.Y. (2003). Fundamentals of Powder Diffraction and Structural Characterization of Materials. New York, NY: Springer Science + Business Media, Inc.
42. Skoog, D.A., Holler, F.G. and Crouch, F.A. (1998). Principles of Instrumentation Analysis. Fifth Edition. Brooks Cole.
43. Bozzola, J.J. and Russel, L.D. (1992). Electron Microscopy: Principles and Techniques for Biologists. Toronto: Jones and Bartlett Publishers.
44. http://www.ualberta.ca/~ccwj/teaching/microscopy/
45. http://www.tulane.edu/~sanelson/eens211/x-ray.htm
46. CRC Handbook of Chemistry and Physics. 55th ed. CRC Press: Boca Raton, FL, 1984-1985; p E-106-E-107.
47. Journal of the European Ceramic Society 8 (1991) 197-213.
48. "Nitrogen ordering and ferromagnetic properties of epsilon-(Fe3 N1+x) (0.10 < x < 0.39) and epsilon-(Fe3 (N0.80 C0.20)1.38)". Leineweber, A., Jacobs, H., Huening, F., Lueken, H., Kockelmann, W. J. Alloys Compds. 316, 21 (2001).
49. "Nonstoichiometric structures during dehydroxylation of goethite". Wolska, E., Schwertmann, U. Z. Kristallogr. 189, 223 (1989).
50. "Crystal structure and cation distribution in titanomagnetites (Fe3-xTixO4)". Wechsler B.A., Lindsley D.H., Prewitt C.T. Am. Mineral. 69, 754 (1984).
51. "å-Fe3N: magnetic structure, magnetization and temperature dependent disorder of nitrogen". Leineweber A., Jacobs H., Huning F., Lueken H., Schilder H., Kockelmann W. J. Alloys Compds. 288, 79 (1999).
52. N.E. Brese and M. O'Keeffe, "Crystal Chemistry of Inorganic Nitrides", Structure and Bonding, Vol. 79, 307-378 (1992).

53. "Powder XRD structure refinements and 57Fe Moessbauer effect study of synthetic Zn1-x Fex Al2 O4 (0< x< 1) spinels annealed at different temperatures". Waerenborgh, J.C., Figueiredo, M.O., Cabral, J.M.P., Pereira, L.C.J. Phys. Chem. Miner. 21, 460 (1994).
54. "A Measurement of Charge Asphericity in Iron Metal". Ohba S., Saito Y., Noda Y. Acta Crystallogr., Sec. A: Cryst. Phys., Diffr., Theor. Crystallogr. 38, 725 (1982).
55. "Crystal structure and magnetic properties of the compound FeN". Suzuki K., Morita H., Kaneko T., Yoshida H., Fujimori H. J. Alloys Compds. 201, 11 (1993).
56. "Chimie Minerale.-Substitution de l`aluminium au chrome dans le chromite de fer bivalent". Chassagneux F., Rousset A. C. R. Seances Acad. Sci., Ser. C 277, 1125 (1973).
57. Swanson et al. Natl. Bur. Stand. (U. S.), Circ. 539 IV, 3 (1955).
58. Natl. Bur. Stand. (U. S.) Monogr. 25 12, 5 (1975).
59. Anya, C., Hendry, A. J. Eur. Ceram. Soc. 10, 65 (1992).
60. Visser, J., Technisch Physische Dienst, Delft, Netherlands. ICDD Grant-in-Aid (1984).
61. "Electric Field Gradients and Charge Density in Corundum, á-Al2O3". Lewis J., Schwarzenbach D., Flack H.D. Acta Crystallogr., Sec. A: Cryst. Phys., Diffr., Theor. Crystallogr. 38, 733 (1982).
62. "Structural properties of nine silica polymorphs". Keskar N.R., Chelikowsky J.R. Phys. Rev. B: Condens. Matter. Mater. Phys. 46, 1-13 (1992).
63. "Crystal-structure calculation with distorted ions". Lacks, D.J., Gordon, R.G. Phys. Rev. B: Condens. Matter. Mater. Phys. 48, 2889 (1993).
64. "Neutron diffraction study of â`-sialon". Van Dijen F.K., Metselaar R., Helmholdt R.B. J. Mater. Sci. Lett. 6, 1101,1102 (1987).
65. "E9: The new high-resolution neutron powder diffractometer at the Berlin neutron scattering center". Toebbens, D.M., Stuesser, N., Knorr, K., Mayer, H.M., Lampert, G. Mater. Sci. Forum 378, 288 (2001).
66. DCALC program. Wagner, T.R.
67. "The refined structure of SrO•2Al2O3". Lindop A.J., Goodwin D.W. Acta Crystallogr., Sec. B: Struct. Crystallogr. Cryst. Chem. 28, 2625 (1972).

68. M. Hillert and S. Jonsson, Report No. TRITA-MAC 399, Royal Institute of Technology; Stockholm, Sweden, 1999.
69. Natl. Bur. Stand. (U. S.) Monogr. 25 20, 91 (1984).
70. Swanson, Tatge. Natl. Bur. Stand. (U. S.), Circ. 539 I, 11 (1953).